QUANTITATIVE IMAGE ANALYSIS OF *IN VIVO* MICROSTRUCTURE AND GROWTH FACTOR EFFECTS IN HYDROXYAPATITE BONE SCAFFOLDS

BY

SAMANTHA JANE POLAK

THESIS

Submitted in partial fulfillment of the requirements
for the degree of Master of Science in Bioengineering
in the Graduate College of the
University of Illinois at Urbana-Champaign, 2010

Urbana, Illinois

Adviser:

Assistant Professor Amy Wagoner Johnson

Abstract

Osteoinductive agents, such as BMP-2, are known to improve bone formation when combined with scaffolds. Microporosity (<20μm) has also been shown to influence bone regeneration in calcium phosphate (CaP) scaffolds. However, many studies use only the term "osteoconductive" to describe the effects of BMP-2 and microporosity on bone formation, and do not assess the degree of healing that occurred. The objective of this study was to quantify the influence of BMP-2 and microporosity on bone regeneration and healing in biphasic calcium phosphate (BCP) scaffolds using multiple measures including bone volume fraction (BF), radial distribution (RBD), and specific surface area (SSA). These measures were quantitatively compared by analyzing micro-computed tomography data and used to formally define and assess healing. An accurate custom image segmentation program was developed that utilizes grayscale values, the periodicity of the scaffold, and 3D spatial features to segment background, bone, and scaffold pixels. This program was used to segment >100 samples, with 900 images each, that were implanted in porcine mandibular defects for 3, 6, 12, and 24 weeks. The assessment of healing presented in this work demonstrates the level of detail possible in evaluating scaffold-guided bone regeneration. The analysis shows that BMP-2 and microporosity accelerate healing up to four-fold. BMP-2 and microporosity were shown to have different and complementary roles in bone formation that effect the time needed for a defect to heal.

To Mom and Dad

Acknowledgments

This work was supported by a grant from the Aircast Foundation (No. S0406R) and by a Research Support Grant award from the Oral and Maxillofacial Surgery Foundation. Some of the work was done in the Imaging Technology Group (ITG) at Beckman Institute which is partially supported by the National Science Foundation (DBI-9871103). The author thanks S. Lan Levengood for her assistance in surgical procedures, sample retrieval, imaging, and histology. The author would also like to thank D. Hoelzle, A. Maki, M. Poellmann, and S. Wilson as well as Dr. M. Wheeler and Dr. S. Clark for their assistance in surgical procedures and sample retrieval, and M. Vogle for histology assistance. The imaging and data analysis was supported in part by the National Science Foundation under Grant no. 0414956. Fellowship assistance was awarded by the University of Illinois at Urbana-Champaign (UIUC) College of Engineering Roy J. Carver Fellowship program and the UIUC Support for Under-Represented Groups in Engineering (SURGE) Fellowship Program.

Table of Contents

Chapter 1. Introduction

1.1 Background and Significance

Bone trauma, degeneration, and disease are relatively common medical maladies. In fact, over 1.5 million bone graft procedures are performed each year in the United States alone (1). Many of these causes are associated with aging, therefore the frequency of bone grafts will increase substantially with the aging population. Thus the annual toll on the health care system will quickly surpass the $2.5 billion currently spent on bone grafts and the $1.5 billion spent on bone graft substitutes in the United States (1-4).

Autografts, or graft tissue from another site on the patient's body, is one of the most common methods for repairing tissue defects (3). While these procedures are standard for defect repair, they are associated with complications and long-term side effects (5,6). In graft harvests from the iliac crest, a common site for autografts harvest, donor site numbness (24%) and pain were frequently reported. Nineteen percent of patients experienced pain that affected their ability to perform household chores, 18% reported pain that limited their recreation, 16% had difficulty walking, and 10% had decreased ability to work. Three and a half years after surgery these complications resulted in overall worse physical health (5).

Allografts, or grafts from donors, are another standard technique used to treat bone defects. While allografts eliminate all problems associated with the harvest site, grafting foreign tissue presents other complications. The procedure increases the risks of disease transmission, immunological reactions (7,8), and death (9-11) and may require the use of immunosuppressant drugs (12). Both allografts and autografts are limited in their usefulness due to a restricted amount of available material.

1.2 Bone Scaffolds for Defect Repair

The need for improved technologies for bone defect repair has been recognized for many years. In 1965 Urist arguably started the modern work on scaffold-based bone replacement and repair when he regenerated bone in a decalcified bone matrix (13). Since then there have been numerous investigations of bone repair strategies using a range of materials and scaffold characteristics. Metals, polymers, and bioceramics have been investigated with a range of scaffold structures(14-19). Research has been performed to elucidate the mechanisms and effects of growth factor delivery to induce and enhance bone formation (20). However, controlling tissue regeneration has proven to be extremely complex and, over forty years after Urist's inital study, autografts and allografts are still the standard techniques for repairing bone defects despite their significant limitations (3).

1.3 Materials

The basic requirements for a bone substitute material are biocompatibility and osteoconductivity, meaning the material does not induce an immune response and that the material encourages the formation of bone on its surface (7,21-23), respectively. Many materials meet these requirements, but two general categories have been the subject of much study. One is polymers, which are typically replaced completely by native tissue. The other is the class of calcium phosphates, which are materials that closely match the composition of native bone and remain relatively unabsorbed, or resorb very slowly.

Many types of both natural and synthetic polymers have been investigated in for use as bone scaffolds including poly (L-lactide), polyglycolide (PGA), collagen, polylactides (PDLA) (23), and chitosan(24). These materials have varying degradation times, mechanical properties, functional groups, density, and surface topography making the selection of a suitable polymer for a specific defect difficult (25,26). Polymers' accelerated degradation rates and degradation

products that can inhibit bone formation make a load bearing and fast healing scaffold not immediately feasible (23).

Due to their physical and chemical properties, hydroxyapatite (HA) and other calcium phosphates (CaP) have been successfully used to repair some bone defects. CaPs are have a composition nearly identical to mineralized bone (7) and are bioactive (form chemical bonds with bone), biocompatible, and osteoconductive (7). CaPs are widely used in dentistry and in reconstruction of simple maxillofacial defects (7,27-29), and they provide a surface to which proteins readily adhere (30). CaP-based constructs can be manufactured with interconnected pores on the order of hundreds of microns, which mimic those seen in native bone, and the scaffold structure can be controlled using advanced materials processing and fabrication techniques(7,9,15,21,31-33).

CaPs have been used in surgeries since the 1950s (34). HA and other CaPs have been widely used as coatings for titanium implants to improve bone/implant interface (35,36). CaPs have relatively slow degradation times and thus are more likely to remain mechanically stable throughout healing. When the material does degrade the products are calcium and phosphate ions, which are conducive to bone growth (37). Like all ceramics, CaPs are brittle, but recent work has shown their ability to integrate with bone at the microscale level which potentially mitigates brittle failure (38).

1.4 Microstructure

The manipulation of scaffold microstructure has also been investigated as a possible mechanism for improving bone formation within scaffolds. Several studies have shown that HA with both macroporosity and microporosity, termed microporous (MP), supports and induces bone growth more effectively than scaffolds with only macroporosity, termed non-microporous (NMP) (7,21,31,39-41). Macroporosity allows for cellular infiltration, transport of nutrients, and

the removal of waste (39,42). The role of microporosity is not as clear. The micropores have been shown to act as drug and growth factor reservoirs (39,42) and to serve as binding sites for proteins that are advantageous for vascularization and bone ingrowth(39,42).

The size of the micropores, topography, and the specific surface area (SSA) created by the micropores is known to influence cell response(8,9,39,43,44). One leading hypothesis for the increased osetoconduction and osteoinduction (the stimulation of progenitors cells to differentiate down osteoblastic lineages) seen in scaffolds with a combination of macro and microscale porosity (multiscale porosity) is related to an increase in SSA. The rationale is that the increase in SSA increases the rate of dissolution of the CaP and increases the precipitation rate of biological apatite. The apatite is thought to interact with native proteins and increase osteoinductivity (15,21). However, this is likely an oversimplification as topography, dissolution/reprecipitation, grain boundaries, surface energies, and protein interactions have all been suggested as mechanisms for cellular response and bone formation(9,39,45-47).

Recent studies show that in addition to increasing bone formation in the macropores, the micropores themselves can serve as space for the bone to form (38). However, the pattern of bone growth between studies is not consistent. Some studies have observed bone formation in the central region of the scaffold (15,48) and others have observed the majority of regenerated bone at the scaffold periphery (49). This inconsistency may be due to the lack of design control when the microstructure of scaffolds is determined by sintering temperatures. Little work has been done to investigate regenerated bone volume or growth patterns in CaP scaffolds with well-controlled, consistent macrostructure and microstructure.

1.5 Growth Factors

The use of bone morphogenetic proteins (BMP) to improve bone growth in scaffolds has been explored with different results (15,38,50,51). BMPs are known to be osteoinductive and to both

recruit undifferentiated cells and to stimulate their differentiation down the osteoblastic lineage (50,52-57). In particular, BMP-2 has been shown to induce bone formation by stimulating chemotaxis, increasing proliferation, and/or differentiation of osteoprogenitor cells (50,52,53,56-58). These responses have been shown to be dose-dependent with nanogram quantities causing chemotaxis and microgram amounts stimulating bone differentiation (52,58-60). Studies of CaP scaffolds have shown BMP-2 to improve bone induction in ectopic sites (40,61), but the influence of BMP-2 on osseous defects has been less clear with contradictory results and location dependent responses (51,52,61). BMP-2 is extremely expensive and in some cases not feasible due to cost, standard doses cost approximately $5000 (62). Many surgeons prefer to use BMP only if an initial surgery was not successful even though its benefits to healing have been shown (62).

1.6 Analytical Methods for Bone Growth Quantification

1.6.1 Tissue evaluation of growth and morphometry using destructive techniques

The most common methods for measuring bone formation and morphometry in CaP scaffolds are histological analysis and scanning electron microscopy (SEM) (15,31,48,49,61). Micro computed tomography (micro-CT) is typically used for qualitative assessment because the nearly identical mineral composition of HA and bone result in similar x-ray attenuations. This makes segmentation of bone and scaffold difficult when using standard micro-CT methods. Histomorphometry is done using representative sections of the sample and the values for volume and morphological features are based on two-dimensional extrapolation (15,48,49,61). Since the entire scaffold cannot be observed, representative sections must be used which results in lost information. Additionally, some of the sample itself is lost during preparation. The visual assessment and comparison of bone via histology and SEM in CaP scaffolds has been described by other researchers as difficult (61).

1.6.2 Common methods of image segmentation

Image segmentation, or computer vision, is comprised of multiple techniques that can be combined to obtain the optimum segmentation results. The techniques can be roughly categorized into one of eight groups: thresholding, region growing, classifying, clustering, Markov Random Field models (MRF), artificial neural networks (ANN), deformable models, and atlas-guided approaches (63). Thresholding divides pixels based on intensities, with the end goal of either maximizing between group variance or minimizing within group variance (64,65). Region growing uses a manually selected seed point and expands upon that location by connecting adjacent pixels with similar intensity. This approach is commonly used for identifying tumors or lesions (63). Watershed algorithms are a kind of region growing which segment images based on the local maxima and minima of the grayscale values of the pixels (66). Classifiers use manually segmented training sets to search for features, or visual and spatial traits, common to each material. The algorithm then uses those features to assign pixels to materials in new images. Common examples of the algorithms used to maximize the likelihood of assigning pixels to the correct material are k-nearest-neighbor (knn), naïve Bayes, and maximum likelihood (ML) (63). Clustering is very similar to classifiers except clustering does not use manually created training sets. Clustering constantly iterates the segmentation, until the best labeling has been achieved using algorithms such as k-means or expected-maximization (63). MRF models use the interaction of neighboring pixels for segmentation but are computationally intense and often results in excessive smoothing, thus blurring borders between materials. ANNs are a form of machine learning that use decision nodes and weight the importance of different features for segmentation. This approach requires training sets but is good at using spatial features in 3D segmentation (63,64). Deformable models require manual interaction. Closed curves are drawn approximately where an edge should be located. The

algorithm then relaxes the curve until an energy minimum has been reached, meaning the internal stretch/bend forces are balanced with the external gradient/edge forces (63). The edge dictated by the clarity and severity of the gradient outside of the curve is balanced, with the goal of creating the smoothest curve. Finally, atlas-guided approaches use knowledge of an object's structure to create a template to identify the desired object. The template or atlas is then warped to fit the object in the experimental image. This technique is also known as image registration (63,67).

1.6.3 Image segmentation in tissue scaffolding

Numerous attempts have been made to segment images of CaP scaffolds, however segmentation of entire scaffolds has not been possible due to a small field of view and due to the similarity in attenuation of the materials (67-71). Several *in vivo* studies have used thresholding to separate bone from CaP scaffolds with mixed results (68,69). One approach used simple thresholding values to differentiate three materials: soft tissue was less than 50% of the maximum grayscale value, bone was 50-68% of the maximum value, and scaffold was greater than 68% (69). However, the bone volume fraction was found to be significantly greater using the micro-CT segmentation than in the validation method, SEM (69). This may be due to a change in attenuation of bone and scaffold throughout the healing process (71). Initially scaffolds attenuate more than bone but over time, as bone mineralizes completely, the difference in attenuation becomes indistinguishable. Somewhat more sophisticated thresholding techniques have been employed as well. Van Lenthe describes a two-step thresholding method with material dilation to reduce the partial voxel effect (68). However, spatial considerations were not used and validation methods were not described.

Atlas-guided or image registration methods have been used to assess scaffold fabrication and to observe *in vitro* degradation (67,70), but have not been used in *in vivo*

studies, to our knowledge. Image registration was used to assess titanium scaffold fabrication and to assess *in vitro* polypropylene fumarate/tri-calcium phosphate scaffold degradation (67). The same technique was used to analyze HA/polymer composites and identify ceramic/polymer interdigitations on the scaffold surface (70).

1.7 Objective of the Thesis

The objective of this study was to evaluate the influence of both microporosity and BMP-2 on bone formation in biphasic calcium phosphate (BCP) scaffolds with both macro and microscale, or multiscale, porosity. We used a custom image segmentation program to quantify bone volume fraction, radial distribution, and specific surface area from micro-CT data sets of scaffolds implanted in porcine mandibular defects. These large data sets contained 900 images per scaffold and over 100 scaffolds were evaluated. Comparisons between treatments were made using multivariate and subsequent univariate statistics, which allowed us to separate the influence of microporosity and BMP-2 on the three measures of bone formation. Comprehensive quantification of bone ingrowth in scaffolds generally presents significant challenges. This study uses an unusually extensive amount of data and a custom images segmentation program to address those challenges. We were able to quantify and compare multiple relevant measures of bone regeneration within CaP scaffolds. This thesis contributes to a fundamental understanding of the role of microporosity and BMP-2 on bone formation in CaP scaffolds, presents a new method for segmenting implanted CaP bone scaffolds, and provides specific information to guide the rationale design of CaP scaffolds for bone replacement and repair.

1.8 Thesis Organization

The thesis is organized as follows. In Chapter 2 the *in vivo* porcine study is described and discussed. Motiviation, methods, results, and a detailed discussion are included. Chapter 3 details the segmentation algorithms developed for use in the study described in Chapter 2. A step-by-step description of the algorithm as well as justification for manually selected parameters and several verification analyses are included. A discussion of the functionality of the algorithms follows. Chapter 4 contains an overall summary and conclusions for all the work presented in this thesis. Future work is also discussed for each of the two main sections of the thesis – (1) effects of microstructure and growth factor and (2) micro-CT image segmentation. An appendix with all of the codes used in segmentation follows Chapter 4, and a list of references is included as the last section.

Chapter 2: *In* vivo Porcine Study

2.1 Introduction

As discussed in Sections 1.4 and 1.5, microporosity and BMP-2 are factors known to improve bone formation in scaffolds. However the specific roles of each factor and their effects in hydroxyapatite (HA) scaffolds with well-controlled macro and microstructures have not been identified. Bone has been shown to integrate into macro and micropores, and BMP-2 has been shown to increase the number of osteocytes present in scaffold micropores (51). The multiscale integration of biological tissue within a hydroxyapatite scaffold could be a means of mitigating brittle behavior of the ceramic scaffold. The possible improvement in mechanical properties and increase in bone formation in scaffolds with microscale bone integration motivate a study of the effects of microporosity and BMP-2 on bone formation. In this *in vivo* porcine study four treatment groups were evaluated for each of four time points: scaffolds with and without microporosity, and scaffolds with and without BMP-2. Scaffolds were implanted in the mandibles of 6 month old pigs for 3, 6, 12, and 24 weeks and then evaluated using micro-CT and histology. The resulting image data was quantitatively analyzed at a level of depth not previously seen.

2.2 Experimental Methods and Materials

2.2.1 Scaffold fabrication and characterization

Scaffold fabrication and characterization follow the same methods used in previous work (32,72-74). The HA powder (Riedel-de Haen, Seelze, Germany) was characterized by Hoelzle and Cordell (32,73) and the deposition solution, or ink, was formulated as described by Dellinger *et al.*, Michna *et al,* and Hoelzle (72,74,75). As received hydroxyapatite (HA) powder was first calcined for 10 hours at 1100˚C in order to reduce the surface area of the powder. The calcined powder was then ball milled with alumina media for 14 hours, which broke up

agglomerates and decreased particle size. After ball milling, the solution was dried for 15 hours at 125˚C to remove moisture.

The mass of the HA powder was used to calculate the quantities of Darvin 821A (R.T. Vanderbilt, Norwalk, CT) and deionized water needed to form the HA ink. Five molar NH_4OH was added until the solution reached pH of 10. The calcined and ball milled powder was added incrementally to the solution with brief sonication between additions. Once all of the HA was incorporated, the solution was mixed on a paint shaker and centrifuged for 1 hour in order to separate and then remove the liquid phase of the solution. The remaining material was returned to the paint shaker. A known mass of the solution was then dried to determine the solids loading of the slurry, which was used to determine the quantity of each remaining additive. The porosity in the microporous samples was introduced using poly-methyl methacrylate (PMMA) microspheres (Matsumoto Microsphere M-100, Tomen America, New York, NY) in the ink as sacrificial porogens. Water, methocel, and 1-octanol were added to both microporous (MP) and non-microporous (NMP) inks to create the rheological properties needed for deposition. After mixing on the paint shaker, 1M HNO_3 was added incrementally to the ink to adjust the rheological properties, which was required to ensure that deposited scaffold rods could span the rods in the previous layer and bear the weight of subsequent scaffold layers. A gelling agent, poly(ethyleneimine) (PEI), was added once the proper viscosity was reached.

Rectangular lattices composed of alternating layers of orthogonal rods were fabricated using micro-robotic deposition such that two cylindrical samples 5 mm in diameter and 8 mm in height would be obtained after machining cylinders out of the sintered lattices (75)]. Ink additives and PMMA were burned out at 900˚C. The lattices were sintered for 2 hours at 1300˚C and then cooled to room temperature. During sintering, 13% of the HA transformed to β-TCP, resulting in biphasic calcium phosphate (BCP) scaffolds, as verified by X-Ray Diffraction (XRD)

(38). Prior to machining, the lattices were embedded in machinist's wax (McMaster-Carr, Robbinsville, NJ), which was burned out at 525˚C for 1 hour. The scaffolds were then sterilized by autoclave.

MP and NMP samples that were not implanted were imaged using SEM analysis prior to implantation in order to visualize microstructural features. The samples were coated with gold-palladium and imaged using a Philips XL30 ESEM-FEG (FEI Company, Hillsboro, OR, USA).

2.2.2 Preparation of gelatin microparticles for rhBMP-2 delivery

Recombinant human BMP-2 (BMP) was incorporated into half of the total MP and NMP samples using crosslinked and lyophilized gelatin microspheres that were suspended in an uncrosslinked gelatin solution as described previously (51,76). To fabricate microparticles, a 10 wt% solution of basic pharmaceutical grade gelatin (isoelectric point 9, Nitta Gelatin Corp, Osaka, Japan) was added to 40˚C olive oil at a volumetric ratio of 1:35. This mixture was cooled to 4˚C and emulsified using a motorized stirrer. The microparticles were rinsed in cold acetone and then washed through stainless steel sieves. Particles 20-50 μm in diameter were crosslinked with 25% glutaraldehyde in 0.1% Tween 80. The reaction was quenched by the addition of 100 mM glycine. The microparticles were washed in ultrapure water and then lyophilized.

The BMP (R&D Systems, Minneapolis, MN) was reconstituted in sterile 4 mM HCl with 0.1% bovine serum albumin (BSA) at a concentration of 0.5 mg/ml. BMP was added to the microparticles at a ratio of 10 μL BMP solution to 1 mg microparticles, ensuring undersaturation, and allowed 2 hours for infiltration. This resulted in a final concentration of 5 μg BMP/1 mg microparticle (77). The BMP loaded microparticles were resuspended in 2 wt% uncrosslinked gelatin at a concentration of 1 mg/45 μL. Then, 45μL was pipetted onto the top face of the

scaffold and allowed to infiltrate the macropores. The final amount of BMP per scaffold was 5 μg. Scaffolds containing BMP were stored at 4˚C until implantation.

2.2.3 Surgical procedure

One hundred and thirty kilogram, male Yorkshire pigs six months of age were used in this animal study. The University of Illinois Institutional Animal Care and Use Committee (IACUC) approved all procedures (#07177) and all IACUC guidelines were followed. Six animals were designated for each time point: 3, 6, 12, and 24 weeks. The animals for each time point were divided into two groups: those to receive scaffolds with BMP and those to receive scaffolds without BMP. Within those two groups MP scaffolds and NMP scaffolds were randomly assigned to the animals. Three CaP scaffolds were implanted in the ramus of each hemi-mandible for a total of six scaffolds per animal. In total, nine samples per treatment group per time point were implanted. The specific treatment groups were designated as follows: MP scaffolds without BMP (MP/No-BMP), NMP scaffolds without BMP (NMP/No-BMP), MP scaffolds with BMP (MP/BMP), and NMP scaffolds with BMP (NMP/BMP). The scaffolds were placed in 5 mm diameter bicortical defects created using a Stryker surgical drill and bone trephine. Animals were euthanized at the pre-determined end points and the mandibles removed.

Initial sedation was achieved using a cocktail of 1.47 mg telazol, 0.09 mg atropine, 2.9 mg xylazine, and 5.9 mg ketamine per kilogram. During surgery animals were maintained under general anesthesia using halothane vaporized in oxygen. A retromandibular incision was made through the skin and continued with a submandibular incision through the subcutaneous tissue. Care was taken to avoid the facial vein and artery. The approach continued to the inferior border of the mandible where the periosteum was reflected and the mandibular cortex exposed. A variable speed surgical drill fitted with a trephine bur (Meisinger, Centennial, CO) was used to create the defects. The drilling was performed under constant irrigation with cold

saline. The scaffolds were press-fit into the defects and the periosteum then closed using interrupted Vicryl™ suture. The muscle, subcutaneous and skin layers were closed using a simple continuous pattern. Analagesics and broad spectrum antibiotics were administered postoperatively. The animals recovered in individual pens and were kept on a soft diet for 7-10 days before returning to a regular dry swine diet.

At the determined end points, the animals were euthanized. The scaffolds were retrieved by first removing the soft tissue using both scalpel and periosteal elevator. The surface around the implantation site was then polished using an EcoMet® 3000 Grinder-Polisher (Beuhler, Lake Bluff, IL) to expose the top faces of the scaffolds. To preserve the entire scaffold, an 8 mm diameter trephine (Meisinger) attached to a standard drill press was used to excise the scaffold under continuous irrigation with cold saline. The excess bone around the scaffold was then sanded away, leaving just the scaffold in order to ensure the highest possible CT resolution.

2.2.4 Histologic Analysis

The histological evaluation was used primarily to verify the presence of healthy bone and demonstrate active bone formation and remodeling by osteoblasts and osteoclasts, and the presence of blood vessels and adipose tissue; histology was not used for quantification. The PMMA embedding methods described by Sterchi and Eurell were followed to prepare scaffolds (78). Scaffolds were fixed in 10% neutral buffered formalin for approximately seven days immediately after micro-CT scanning. The samples were dehydrated in increasing concentrations of ethanol and infiltrated with methylmethacrylate (MMA) monomer. Once polymerized, the samples were sectioned along the longitudinal axis to a thickness of 500 µm using a Buehler Isomet 100 diamond saw (Buehler, Lake Bluff, IL). Next, sections were fixed onto acrylic slides and ground and polished to a thickness of 150 µm. Images were recorded

using an IX51 light microscope (Olympus, Center Valley, PA) after staining with Sanderson's Rapid Bone Stain (Surgipath, Richmond, IL) followed by an acid fuchsin counterstain.

2.2.5 Statistical Analysis

Statistical analysis was done using a multivariate analysis of variance (MANOVA) followed by univariate analysis (ANOVA), and post-hoc Bonferroni tests. The MANOVA analyzes the groups of dependent variables simultaneously, BF, RBD, and SSA, in order to quantify the overall effect of the independent variables, BMP, microporosity, and time, on all measured aspects of bone growth. ANOVA was next used to identify which treatments were most influential to each of the individual measures of bone growth. The Bonferroni test accounts for the increased chance of incorrectly detecting a significant difference, which can occur as the number of levels of the independent variables increases (79). Here, microstructure and growth factor each had two levels and time had four.

The parameter eta^2 was used to rank the influence that the independent variables had on the dependent variables that were previously found to be significant (80,81). Eta^2 is the variance within a dependent variable introduced by each independent variable. Observed powers (OP) were taken into consideration and direct and individual comparisons between each of the four experimental groups, - MP/No-BMP, NMP/No-BMP, MP/BMP, and NMP/BMP - were not made due to low OPs, less than 0.70. The OP indicates the tendency to detect a statistical difference between groups should a difference exist. In other words, with a low OP differences that truly exist may not be detected. Outliers were determined using standard calculations of the interquartile range and were removed prior to the statistical analysis.

Significance in the MANOVA was determined using Pillai's Trace with $p<0.05$, unless otherwise indicated. Pilliai's trace compares the between group and the total variance in order to determine significance. Significance in the ANOVA was also set at $p<0.05$ unless otherwise

indicated. The statistical analysis for each measure of bone growth describes first the main effects, the influence of microstructure and the influence of growth factor, and then considers how microstructure and growth factor vary over time. Therefore, all samples in the study were included when describing the main effects of microstructure and the main effects of growth factor. For example, when quantifying MP scaffolds, data for MP scaffolds both with and without BMP and at all four time points are included. This is standard procedure for a multi-way ANOVA (80).

Error was reported as the standard error of the mean. The analysis was done using the software package, PASW Statistics 18® (SPSS Inc. Chicago, IL, USA), and figures were generated using OriginPro 8.1 (OriginLab, Northampton, MA, USA).

2.2.6. Quantitative analysis using micro computed tomography

2.2.6.1 Micro-CT imaging parameters

Scaffolds were stored in refrigerated phosphate buffered saline (PBS) until they were scanned using micro computed tomography (micro-CT) (Skyscan 1172, Aartselaar, Belgium), which occurred between one and twelve hours after harvest. A voltage of 75kV, current at 100 mA, and an aluminum filter were used in all micro-CT scans. Projection images were taken at 0.4 degree increments over 180 degrees. Bright and dark field measurements were taken for every sample to establish a baseline. Depending on the size of the excised sample, voxel size was 10-17 µm with 1048 x 2000 pixels per image for 10 µm voxel size and 524 x 1000 pixels per image for 17 µm voxel size. The resolution of the micro-CT scanner allowed for visualization of bone in the macropores only, not in the micropores. Prior to segmentation and analysis the images were reconstructed by NRecon software (Skyscan). Materials with higher attenuation appeared brighter in reconstructed images. As manual segmentation of such a large data set

was not feasible, an automated segmentation program was developed. The program is described in detail in Chapter 3.

2.2.6.2 Image pre-processing and segmentation

Prior to segmentation, the 900-image data sets were imported into the visualization software package, Amira®(Visage Imaging GmbH, Berlin, Germany), and background noise was minimized with brightness and contrast filters. Bone outside of the scaffold at the defect margin, referred to as a bone ring, was cropped in order to prevent over estimation of bone. Cropping was done by manually selecting the scaffold region in multiple images throughout the sample and interpolating between these images. However, due to the scaffold removal process (2.2.3), the scaffold was not perfectly cylindrical. Therefore, using this method, not every image was cropped correctly leaving background noise outside of the scaffold lattice, which will also be referred to as the region of interest (ROI). We refer to this volume of background noise as the "halo region" (Fig 3.2b). The halo was removed in a later step (see 3.2.1 for details). Finally, each scaffold was rotated such that the orthogonal rods were aligned with the Cartesian axes defined by the software.

2.2.6.3 Image post-processing

Once segmented, the images were imported back into Amira®. Half of each scaffold, divided along the long axis, was used for quantification. Excision of the scaffold from the mandible occasionally damaged one or two scaffold rods immediately adjacent to the defect margin, i.e. at the scaffold/bone interface. Bone appeared to grow into the scaffold from the defect margin, therefore including damaged regions would result in an underestimation of bone volume and an inaccurate representation of the radial bone distribution. Thus a fully intact, half cylinder was used for the analysis of all of the scaffolds.

2.2.6.4 Quantification of bone using segmented data

Bone regeneration was quantified using three measures of the segmented data: bone volume fraction (BF), radial bone distribution (RBD), and bone morphology via specific surface area (SSA). BF was defined as the fraction of macropore space occupied by bone, or the total volume of bone divided by the total macropore volume, equation (1).

$$BF = \frac{\sum B_i}{\sum M_i} \qquad (1)$$

Where B = bone volume

M = macropore volume

Bone distribution could not be characterized strictly using the radial position. The orthogonal lattice combined with the cylindrical geometry of the scaffold caused the amount of space available for bone ingrowth at a given absolute radial position and angle to vary not only with respect to the lattice, but also from sample to sample (See Fig. 2.3). To resolve this issue and make meaningful comparisons, the distribution of bone in the scaffold macropore space was described using the relationship between cumulative volume fraction of bone and cumulative volume fraction of macropores measured from the absolute center of the scaffold to the perimeter, equation (2). The RBD was then defined as the fraction of available macropore space that contained half the total volume fraction of bone. RBD as defined ranges from 0 to 1, where 0.5 indicate a uniform distribution of bone. Values less than 0.5 indicate a concentration of bone towards the center of the scaffold and values greater than 0.5 indicate bone concentrated on the perimeter of the scaffold.

$$RBD = \frac{\sum_0^i M_i}{\sum M} \qquad (2)$$

Where i = the radius at which half the bone was contained

M = macropore volume at each radius

SSA was defined as the surface area to volume ratio of bone. SSA has been considered a measure of the metabolic and remodeling activity of bone tissue and thus provides insight into the level of cellular activity of the tissue (31,82,83). The interface area between bone and scaffold was excluded for this measure based on the assumption that cells would not view this interface as one that could be readily remodeled.

2.2.6.5 Definition and criteria for healing

The segmented data and subsequent statistical analyses (see 2.2.5) were also used to define and quantify and compare healing. For a defect to be healed, the BF had to reach steady-state, i.e. no change with time, and the RBD had to be within 10% of the optimal value, RBD = 0.5. Thus, the RBD had to be between 0.5 and 0.6 for the defect to qualify. Steady-state, for any dependent variable, was defined as the first time point at which the variable had a statistically similar value to both the previous and the subsequent time points *and* those two points were statistically similar. This approach was used for BF because, in contrast to the RBD, the specific optimal value was not known. The healing rate or time required to complete healing was the time at which the BF had reached steady-state *and* the RBD reached a value less than 0.6. No criterion for healing was included for the SSA because this was associated more with remodeling.

2.3 Results from *in vivo study*

2.3.1 Characterization of scaffolds and bone tissue

2.3.1.1 Scaffold characteristics

The cylindrical HA scaffolds had a diameter of 5mm and a height of 8mm. Rod diameter was 394µm. Within a layer, the macropore size was 753µm in-plane and 646µm out of plane, measured from rod center-to-center. NMP scaffolds were made with solid rods and MP samples were made with rods containing 50% nominal microporosity (Fig. 2.1).

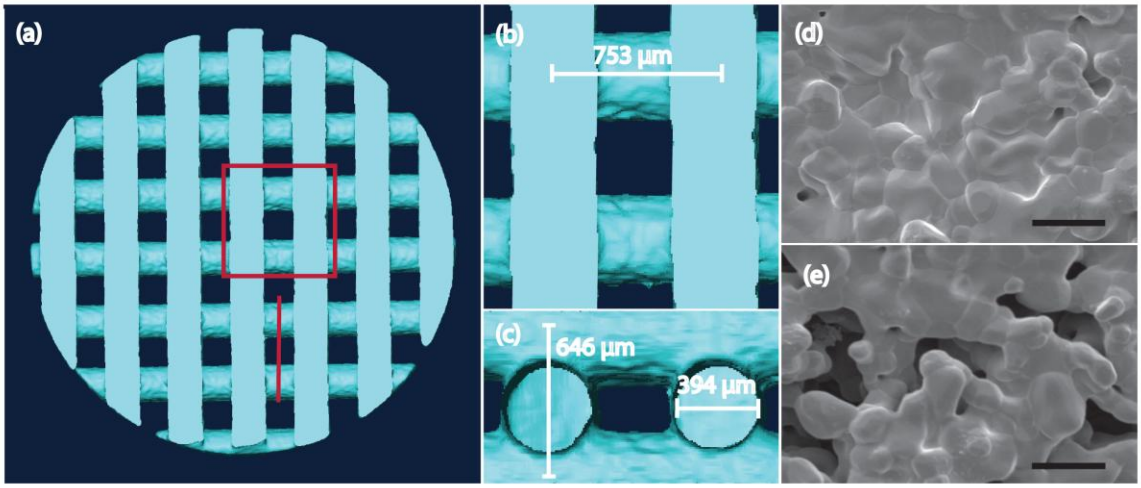

Figure 2.1. Scaffold architecture and microstructure. (a) Rendering of scaffold micro-CT data showing architecture. The red box is shown at higher magnification in **(b)** and the slice indicated by the red line is shown at higher magnification in **(c)**. **(d)** and **(e)** SEM images of the surface of a NMP and MP scaffold rod, respectively. The scale bar indicates 5 µm.

2.3.1.2 Histologic characteristics

Histologic results suggest that normal, healthy bone was present in the scaffold at all time points. Bone, osteoid, and vasculature were present throughout. Osteoblasts, osteoclasts, and osteocytes were also seen as were typical signs of bone formation and remodeling such as scalloped edges on the bone surface (Fig. 2.2).

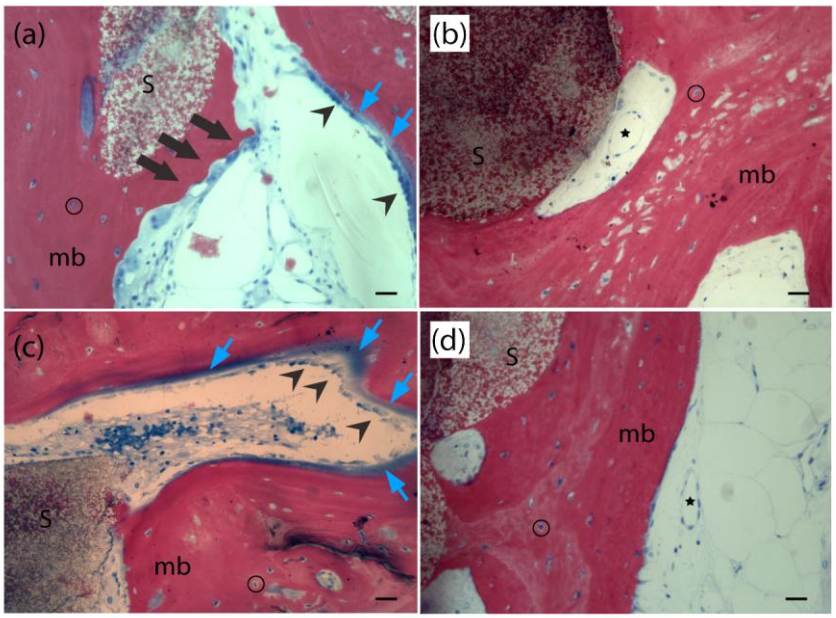

Figure 2.2. Representative histology images showing bone in scaffold (S) macropores. Scale bars indicate 10µm. **(a)** A scalloped edge with osteoclasts actively remodeling the surface ( ). Osteoblasts lining the bone surface ( ) with osteoid beneath ( ). Osteocytes in lacunae ( ) within mineralized bone (mb). **(b)** Scaffold and mineralized bone with blood vessels ( ) for nutrient and waste transport. **(c)** A line of osteoblasts and osteoid, as well as mineralized bone and osteocytes in lacunae. **(d)** Blood vessel near mineralized bone and osetocytes in lacunae. Mineralized bone is pink/red, soft tissue is blue, osteoid is blue/purple, cell nuclei is dark blue, and cytoplasm is light blue.

2.3.1.3 Bone distribution characterization

The distribution of bone throughout the sample was used as a measure of bone formation and as an important measure of the amount of healing. The volume fraction of bone alone does not give any information about where the bone is located or what degree of healing has taken place. A uniform distribution of bone is desirable because it suggests that the system is fully vascularized and that it is more similar the native bone as compared to a scaffold with bone only at the perimeter or center of the scaffold, for example. Figure 2.4 shows reconstructions of micro-CT data for two samples. The MP sample shows a uniform distribution

of bone throughout the scaffold (Fig. 2.4a). In contrast, the NMP sample shows bone concentrated at the periphery (Fig. 2.4b).

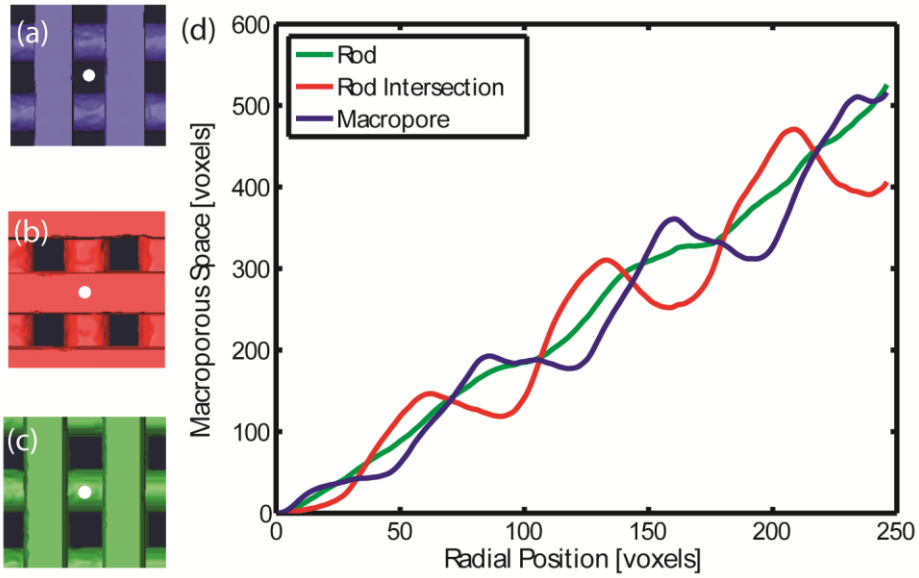

Figure 2.3. Micro-CT data showing the available macropore space for bone at the absolute center of a representative scaffold. A shift in the lattice relative to the absolute center of the scaffold causes a variation in the amount of space available for bone as a function of radial distance from the center. For **(a)** the absolute center is in a macropore; for **(b)** it is centered on an intersection of the orthogonal rods; and for **(c)** it is centered on a rod of one orientation. The shift results from the machining process. **(d)** A plot of the available macropore space versus radial position, with the center of the scaffold at the origin. Note how the macropore space for each case oscillates, because of the periodicity of the scaffold, and is equal at any given position purely by chance.

The radial bone distribution (RBD) was expressed as a single value, defined as the volume fraction of macropore space that contains half of the volume fraction of bone. The rationale for this somewhat unconventional representation of distribution follows. The cylindrical scaffolds to be implanted were machined from a block lattice with no attempt to align the center of the cylinder with the periodic structure of the block. As a result, the absolute center of the scaffold varied relative to the unit cell (Fig. 2.3a-c), which varied the amount of macropore space available at the same absolute radial position (Fig. 2.3d). Thus, RBD could not be defined in terms of absolute radial position.

To determine the RBD, the distribution of bone was represented in a plot of the cumulative bone fraction versus the cumulative macropore fraction (Fig.2. 4c and d) with the center of the scaffold at the origin and the perimeter at 1. The RBD in Figure2. 4c and d is the cumulative macropore fraction at the cumulative bone fraction equal to 0.5, shown by the dotted lines. For these specific data, the RBD for the MP scaffold is 0.51 (Fig. 2.4c), quantitatively indicating an almost perfectly uniform bone distribution. The RBD for the NMP scaffold is 0.79 (Fig. 2.4d), quantitatively indicating that bone is concentrated toward the perimeter of the scaffold. This convention was used to quantify the bone distribution for all samples and was also used in the criteria to define healing.

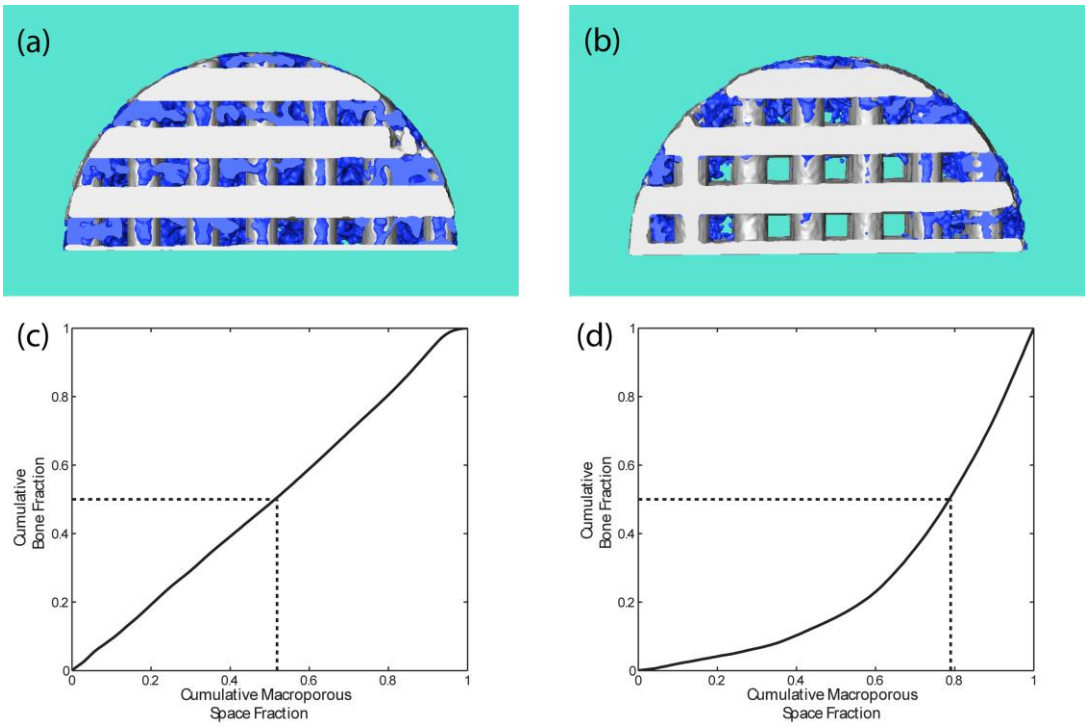

Figure 2.4. Images and plots showing the distribution of bone in implanted scaffolds. (a) Rendering of micro-CT data to show the distribution of bone in a MP scaffold with RBD = 0.51. **(b)** A rendering of the bone distribution in a NMP scaffold with RBD = 0.79. **(c)** and **(d)** show plots of cumulative bone fraction vs cumulative available macropore space; **(c)** is the corresponding plot for the MP scaffold in **(a)** and **(d)** is for the NMP scaffold in **(b)**.

2.3.2 Multivariate analysis (MANOVA) shows that microstructure is most influential independent variable

The MANOVA was used to identify the factor most influential, microporosity, BMP-2, or time to the process of bone formation. A MANOVA is used when multiple dependent variables are measured in a study [54]. Thus, all three measures of bone formation (BF, RBD, SSA) were considered simultaneously in the analysis. Surprisingly, microstructure was more influential to bone regeneration than was time or the potent osteoinductive factor BMP-2. Rank of influence following microstructure was growth factor, time, and finally the interaction between growth factor and time (growth factor x time). The OP for the other pair-wise interactions, microstructure x time and microstructure x growth factor, were low (Table 2.1). Therefore significance, if it existed, was not likely to be detected. Generally speaking, a significant difference will not be detected if it is not present, for any OP, but it can be missed for low OP. As a rule of thumb, OP should be greater than 0.80 or 0.90 in order to be able to conclude that there truly is no significance (84).

Table 2.1. Observed Power from the MANOVA

	Microstructure	Growth Factor	Time
Microstructure	0.999	0.311	0.338
Growth Factor		0.982	0.810
Time			0.994

Linear correlations between dependent variables were also determined using MANOVA. BF and SSA had the strongest correlation at R^2 = -0.683, RBD and BF had an R^2 of -0.372, and RBD and SSA had the weakest correlation at R^2 = 0.241. The correlation between BF and SSA was consistent with bone filling the macropore space; as bone volume increased the trabeculae thickened, which resulted in a lower SSA. The weak correlation between RBD and BF suggests that evolution of the RBD was not due simply to an increase in BF. The dependent variables were analyzed in more detail using the univariate analysis.

2.3.3 Univariate analysis (ANOVA)

ANOVA, followed by t-tests, was done in order to identify which of the scaffold design factors, microstructure and growth factor, were significant for each measure of bone formation. The relative importance of each factor on separate bone measures was also identified. As stated in Section 2.2.5, the term "main effect" refers to the data collected from all samples, i.e. a statement about the main effect of BMP refers to all samples with BMP, regardless of the samples' porosity or the implantation time. Unless otherwise stated, all results refer to main effects as the OP of individual treatment groups (BMP with MP, etc) was not high enough to confidently discuss differences.

2.3.3.1 General effects of time

Time was significant for all three measured variables. However, the significance was most often between 3 weeks and the later time points and influenced all treatment groups in the same manner. Therefore the influence of time will not be discussed independent from other factors.

2.3.3.2 Bone volume fraction (BF)

Microporosity significantly influenced the BF but BMP did not, based on the univariate statistical analysis of main effects (Section 2.2.5). The BF was greater for MP samples as compared to NMP samples with BFs of 0.385 ± 0.016 and 0.337 ± 0.016, respectively (Fig. 2.5). BMP and No BMP treatments had statistically similar BFs of 0.348 ± 0.013 and 0.375 ± 0.016, respectively.

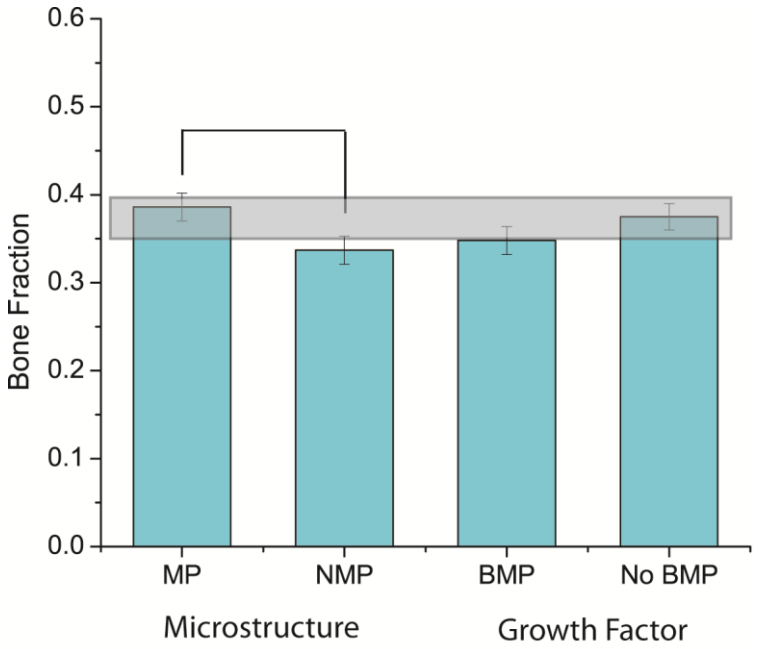

Figure 2.5. Main effects of microstructure and growth factor on bone fraction. The main effect of microstructure is significant; MP samples had a higher bone volume fraction than NMP samples. In contrast, the main effect of growth factor is not significant; BMP and No BMP samples had statistically similar bone fractions. The grey box represents the typical bone fraction of healthy porcine trabecular bone (83,85,86).

The influence of microstructure and growth factor were also analyzed with respect to time. BF for MP samples was statistically similar across all time points (Fig. 2.6a), indicating that these samples had reached a steady-state BF by 3 weeks. The general trend was an increase in BF up to 12 weeks and then a slight decrease at 24 weeks. The NMP group followed the same trend as MP however, BF was statistically different between 3 and 6 weeks, 3 and 12 weeks, and 3 and 24 weeks; NMP samples reached steady-state BF by 12 weeks (Fig. 2.6a, Table 2.2). MP samples also had higher BF at all time points compared to NMP samples, though the data did not satisfy the criterion set for significance ($p<0.05$). However, MP had a significantly greater BF than NMP at 3 weeks with a slightly relaxed significance criterion of $p=0.061$.

Like the MP samples, BMP samples also showed no statistical difference in BF over time indicating that samples in this group had also reached steady-state by 3 weeks (Fig. 2.6b, Table

2.2). In contrast, the No BMP samples showed significantly lower BF at 3 weeks as compared to 12 and 24 weeks and at 6 weeks compared to 12 weeks (Fig. 2.6b). The No BMP group may not have reached steady-state during the study. Across the treatments at a given time point, BMP and No BMP samples were different at 12 weeks, but were similar again at 24 weeks. The growth factor x time interaction was apparent from data in Figure 2.6b.

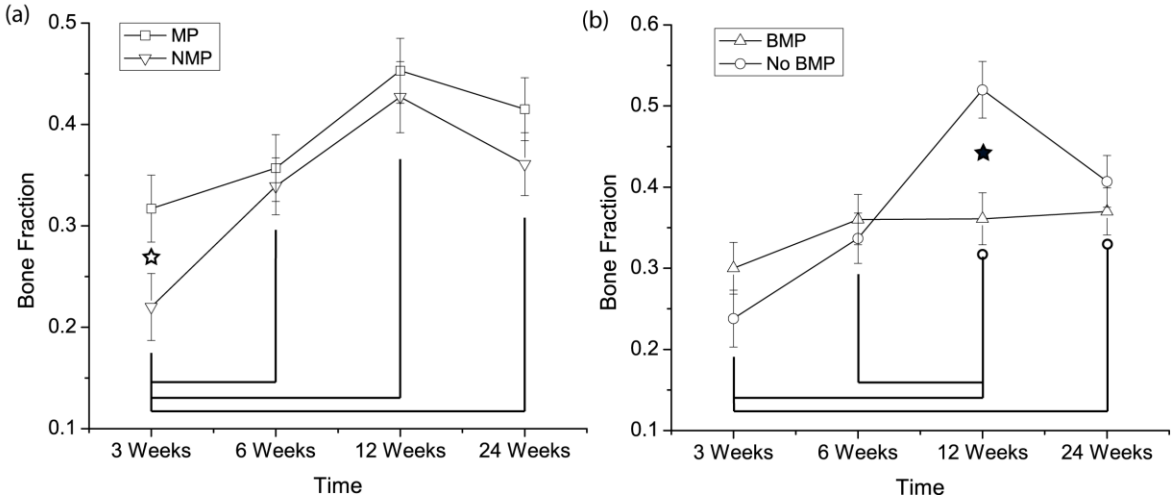

Figure 2.6. Results of analysis of volume fraction of bone in macropores as a function of time. (a) There were no differences in BF in MP across all time points. The open star indicates that with a slightly relaxed significance criterion, MP and NMP samples were different at 3 weeks (p=0.061). However, 3 week NMP samples had a smaller BF than NMP samples at all other time points. **(b)** There were no differences for BMP samples across time. However, 3 week No BMP samples were different from 12 and 24 week samples and BF at 6 weeks was different from 12 weeks. At 12 weeks, No BMP samples had a higher BF than BMP samples did.

2.3.3.3 Radial bone distribution (RBD)

Both microstucture and growth factor significantly influenced the RBD in the analysis of main effects; both treatments resulted in a more uniform bone distribution, which corresponds to a numerical value of RBD closer to the perfectly uniform 0.5. MP samples had a RBD of 0.563 ± 0.01 and NMP samples had a RBD of 0.637 ± 0.01 (Fig. 2.7). The RBDs for BMP and No BMP samples were 0.577 ± 0.011 and 0.623 ± 0.01, respectively (Fig. 2.7).

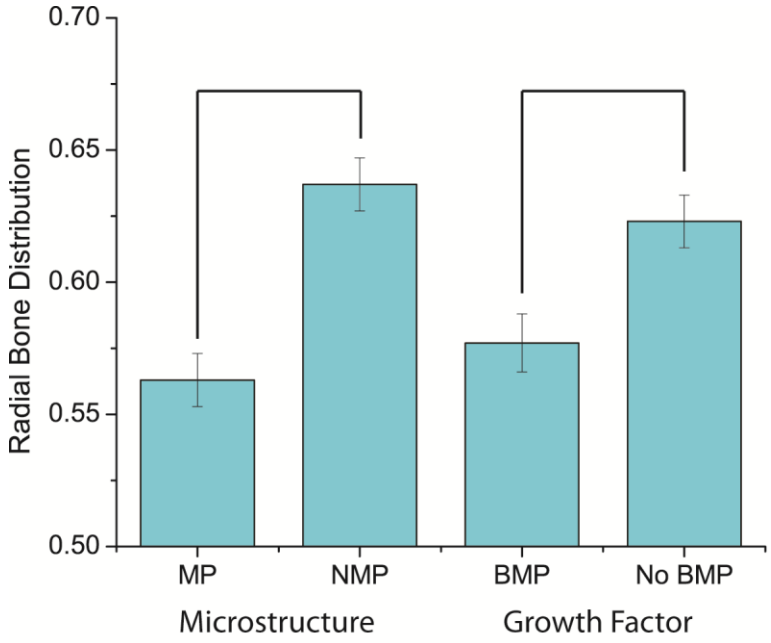

Figure 2.7. Main effects of microstructure and growth factor on radial bone distribution. The main effects of microstructure and growth factor on RBD were both significant for RBD and resulted in a more uniform distribution of bone. MP samples had a lower RBD as compared to NMP and BMP samples had a lower RBD than No BMP samples. These results indicated that MP and BMP samples had nearly uniform bone distributions while NMP and No BMP samples had the bone distributed more toward the perimeter of the scaffold.

The effect of microstructure and growth factor on RBD over time is shown for microstructure in Fig. 2.8a and for growth factor in Fig. 2.8b. For MP samples, RBD was different only between 3 and 12 weeks, while for the NMP samples RBD was different between 3 and 12 weeks and 3 and 24 weeks (Fig. 2.8a). MP reached steady-state RBD by 6 weeks and NMP by 12 weeks. MP and NMP samples satisfied the healing criterion which required a RBD < 0.6 at 6 and 12 weeks, respectively (Fig. 2.8a, Table 2.2). However, in NMP samples RBD increased to just over 0.6 at 24 weeks making time for completion of the healing criterion less certain. Within a time point, the RBD was less for MP than NMP at all time points, but differences were only significant at 3 and 6 weeks (Fig. 2.8a). The significance at 12 weeks was $p=0.059$, which falls just outside of the criterion set for significance ($p<0.05$). MP and NMP generally followed the

same trends with time such that RBD decreased with time up to 12 weeks and then remained the same or increased slightly at 24 weeks. No interactions with time were detected.

For both BMP and No BMP samples, the RBD was different only between 3 and 12 weeks within a treatment. Thus, BMP and No BMP both reached steady-state RBD at 12 weeks. However, they satisfied the criterion of RBD < 0.6 at 6 and 12 weeks respectively (Fig. 2.8b, Table 2.2). No BMP samples had an increase in RBD at 24 weeks such that those samples no longer satisfy the healing criteria (Fig. 2.8b, Table 2.2). While BMP samples had lower RBD as compared to the No BMP samples at all time points, samples only differed significantly at 6 weeks (Fig. 2.8b). These data shown in Figure 8 suggest that microstructure affected RBD more than the BMP since more differences were seen in the MP versus NMP data as compared to the BMP versus No BMP data.

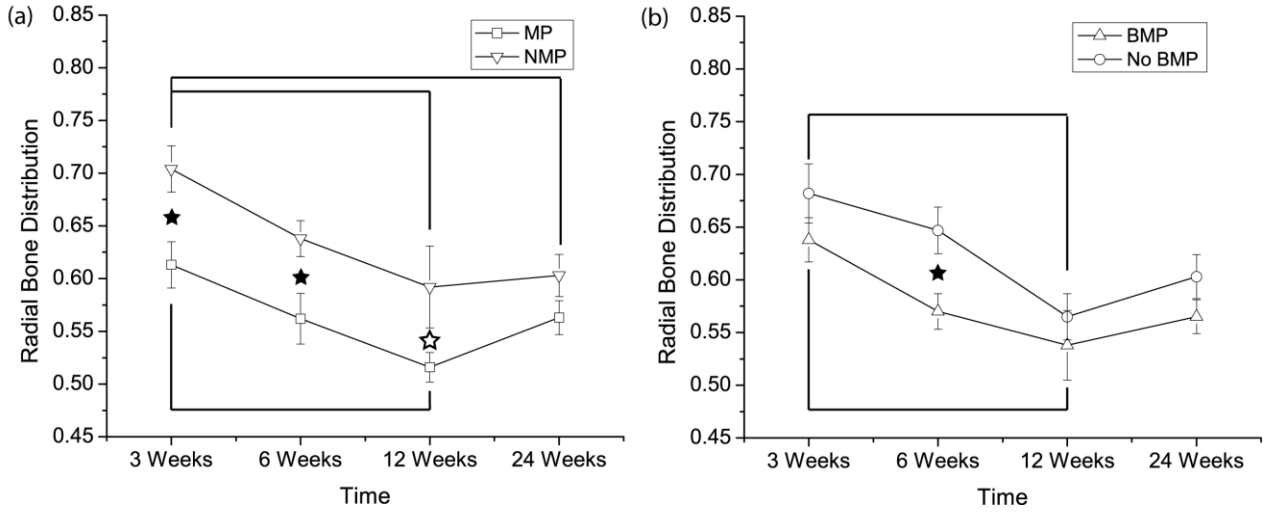

Figure 2.8. Comparisons of the radial bone distribution (RBD) over time for MP and NMP samples (a) and between BMP and No BMP samples (b). **(a)** MP samples had a relatively constant RBD with the only difference between 3 and 12 weeks. NMP samples differed between 3 and 12 weeks and 3 and 24 weeks. At 3, 6, and 12 weeks MP samples had a lower RBD than NMP (p=0.058 for 12 week). This indicates that while the RBD of NMP samples eventually reached an equivalent RBD as compared to MP samples; MP samples had a more consistent and more uniform RBD at earlier time points. The open star indicates a p-value outside the significance criterion, but very close to significant. **(b)** The RBD for BMP and No BMP samples both differed only between 3 and 12 weeks. The only difference between treatments was at 6 weeks.

2.3.3.4 Bone specific surface area (SSA)

For the SSA, the BMP treatment was significant (Fig. 2.9a), but neither microstructure nor any interactions showed significant differences. The BMP treatment resulted in a higher SSA than No BMP, with SSA of 18.492 ± 0.701mm^{-1} for BMP samples and 15.856 ± 0.659mm^{-1} for No BMP samples (Fig. 2.9a).

Both BMP and No BMP samples showed a significant decrease in SSA with time (Fig. 2.9b). For BMP, 3 weeks was different from 12 weeks, and for No BMP 3 weeks was different from 6 and 24 weeks. The BMP samples had a consistently higher SSA across time, though the difference was only significant at 12 weeks (Fig. 2.9b). Both BMP and No BMP samples reached steady-state SSA at 12 weeks (Fig. 2.9b).

2.3.3.5 Comparison of healing for different treatments

When the results are viewed as a function of time, rate of bone regeneration and the notion of "healing" can be summarized (Table 2.2). MP and BMP samples reached a steady-state BF by 3 weeks and had achieved the optimal RBD by 6 weeks (Fig. 2.6, 2.8, Table 2.2). Thus, defects with the MP and BMP treatments had healed by 6 weeks. NMP samples required 12 weeks to reach a steady-state BF and No BMP samples required at least 24 weeks (Fig. 2.6). Both NMP and No BMP samples met the criterion for RBD at 12 weeks, and exceeded the optimum RBD at 24 weeks (Fig 2.8, Table 2.2). Thus healing occurred in NMP samples by 12-24 weeks and by at least 24 weeks for No BMP samples.

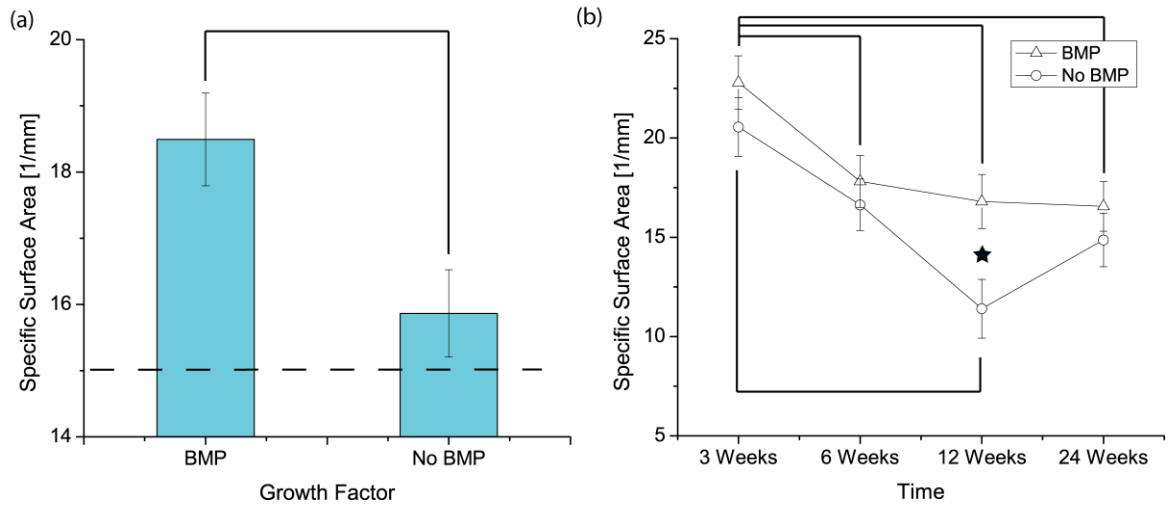

Figure 2.9 The main effects of growth factor (a) and effects across time (b) for specific surface area (SSA). (a) BMP samples had a greater SSA than No BMP samples. The dashed line represents the average porcine mandible trabecular SSA at maturity, 15 mm^{-1} (85). **(b)** BMP had higher SSA at all time points, though the difference was only significant at 12 weeks. No BMP samples had a lower SSA at 12 weeks than at 3. BMP samples at 3 weeks had a higher SSA than at all other time points. At 12 weeks BMP samples had higher SSA than No BMP samples.

2.4 Discussion of *in vivo* study

2.4.1 Microporosity and BMP-2 influence bone regeneration in different ways

Analysis of main effects clearly showed that microporosity and growth factor significantly influence regeneration in different, but perhaps complimentary, ways. Specifically, microporosity significantly increased BF (Fig. 2.5), but did not influence SSA. In contrast, growth factor significantly increased SSA (Fig. 2.9a), but not BF (Fig. 2.5). Both growth factor and microporosity made the bone distribution more uniform (Fig. 2.7). The lack of significant influence of BMP-2 on BF is of particular note given that BMP-2 is a well known osteoinductive growth factor (50) and other researchers have shown an increase in bone volume in the presence of BMP-2 (15,31,87).

The most important result from the analysis of the main effects was with respect to the RBD. The analysis showed early and more uniform bone growth in MP and BMP scaffolds as compared to NMP and No BMP (Fig. 2.7). In fact for MP and BMP, the bone distribution at

steady-state was almost perfectly uniform (i.e. RBD ~0.5). The NMP scaffolds and the No BMP scaffolds had a much less uniform distribution of bone, with the RBD above 0.60, indicating that bone concentrated toward the defect margins up until 12 weeks (Fig. 2.7). It is questionable if No BMP and NMP scaffolds can maintain the optimum RBD, however, as by 24 weeks No BMP and NMP scaffolds had a RBD slightly above 0.60 (Fig. 2.7). To our knowledge few, if any, researchers have characterized the distribution of bone to this degree, yet such an analysis is clearly important to quantifying and understanding bone regeneration. The results from the RBD analysis led us to conclude that, in addition to accelerating healing, BMP-2 and microporosity may increase the size of defect that these scaffolds can effectively repair and therefore contribute to overcoming one of the significant barriers in bone tissue engineering: healing critical size defects.

The analysis of SSA also revealed important results. SSA was influenced by growth factor, but not by microstructure, and scaffolds with BMP had a higher SSA than scaffolds without (Fig. 2.9a). Increased specific surface area has been previously linked to remodeling and metabolic and cellular activity (14,82,83). SSA measured in scaffolds without BMP matched well with accepted values of porcine trabecular bone, 11.3-15.2 mm^{-1} (85,86). However, SSA of bone in scaffolds with BMP was slightly above the typical range (Fig. 2.9a), meaning it was more spindle-like than average porcine trabecular bone. Thus, we postulate that BMP increased the remodeling activity of the cells within the scaffold.

The multivariate analysis showed that BF and RBD were very weakly correlated, with a correlation coefficient of -0.372, and therefore relatively unrelated. This suggests that microporosity did not induce a more uniform distribution simply by increasing the volume of bone. Instead, the microporosity appeared to ensure that a given bone volume was distributed more uniformly. The effect of including microporosity in a scaffold could be summarized as

increasing BF as compared to a NMP scaffold - but with the same level of metabolic activity - and promoting a more uniform distribution. The discovery that different factors of bone formation were affected independently greatly increases researchers' ability to tailor scaffolds for individual people and defect sites.

2.4.2 Healing is accelerated in the presence of microporosity and BMP-2

When the results are viewed as a function of time, we can compare the rate of "healing" in the presence of microporosity or BMP-2. Time for healing is summarized in Table 2.2. To our knowledge, the notion of healing is neither well-specified nor well-characterized in the literature. Results are typically discussed in terms of scaffold osteoconductivity, which refers to the material's ability to support bone formation on its surface, but is not specifically associated with any particular measured variables. The most commonly measured variable is bone volume. However, this parameter does not describe the extent of "healing" as target values are unknown for a given system. We argue that the assessment of the efficacy of a scaffold should include a measure of healing quantified by multiple measures of bone formation.

Both MP and BMP are considered healed by 6 weeks, NMP was healed between 12 and 24 weeks, and No BMP required at least 24 weeks to heal (Fig. 2.6, 2.8, Table 2.2). The time for healing for the NMP samples was less certain as BF reached steady-state and the RBD satisfied the criterion at 12 weeks, but then the RBD increased by 24 weeks with the standard error falling just inside the 0.6 limit. Steady-state for RBD was reached in all cases by 12 weeks. Steady-state for SSA was also reached at 12 weeks for BMP and No BMP samples. Based on the arguments above, we conclude that healing is accelerated in the presence of microporosity or BMP-2. In fact, healing was at least twice as fast for BMP and MP samples as compared to NMP and four times as fast as compared to No BMP samples (Table 2.2).

Table 2.2 Defect healing time

	Time to steady-state BF	Time to RBD < 0.6	Defect healing time
BMP	3 weeks	6 weeks	6 weeks
No BMP	>24 weeks	12 weeks	>24 weeks
MP	3 weeks	6 weeks	6 weeks
NMP	12 weeks	12-24 weeks	12-24 weeks

2.4.3 Potential mechanisms of influence

The difference between the effects of microporosity and BMP on the three measures of bone formation (Fig. 2.5-2.9) may be explained by considering the potential mechanisms of influence for each factor. BMP is known to act in a dose-dependent manner with microgram quantities resulting in cell differentiation and nanogram doses in cell chemotaxis (58-60,88,89). At the concentration used in our study, approximately 100 μg/mL, BMP would be more likely to induce differentiation for cells that were already present at defect site rather than attracting them to the site through chemotaxis. Even if up to 80% of the BMP was released in a burst within one day of implantation, as was observed by Morgan and Yamamoto for a similar delivery system (77,90), near microgram quantities of BMP would still remain bound to the gelatin microparticles within the scaffold macropores.

Our data and research in the literature indicate that the role of BMP was to affect the rate of growth and maturity level of bone seen in the scaffolds. BMP samples had constant BF across all time points, though the radial distribution became more uniform and SSA decreased with time. These results imply that at early time points the bone concentrated at the periphery had many spindles (higher SSA), which is commonly seen in highly metabolically active new growth (82,91,92). However, over time it not only grew into the center of the defect, but also

became more mature and less metabolically active bone (lower SSA). A decrease in metabolic activity with time has been observed in previous studies (14) and SSA has been reported to reach a steady-state level in pigs after approximately 10 weeks after birth (85).

Microporosity has been shown by others to improve osteoconductivity, and in some cases impart osteoinductivity, in CaP scaffolds (21,31,40,41). There is some direct evidence and also speculation as to why this occurs. Some argue that micropore connection size is a critical factor with small connection sizes resulting in lower rates of bone formation (14). Others believe that the microstructure increases the surface roughness that, in turn, increases attachment, proliferation, and cell differentiation (93,94). Still others point to enhanced precipitation of biological apatite following local scaffold dissolution as a potential mechanism (15). The latter idea was supported by the detection of calcium in newly formed bone that came from the implanted CaP scaffolds, indicating that the calcium from the scaffold participates directly in bone formation (49). In addition, microgram quantities of calcium from CaPs have been measured in buffer and in physiologic solution almost immediately upon immersion, with equilibrium between 5 and 20 hours later (20,42), suggesting that this mechanism is important at very early stages of bone formation in CaP scaffolds.

In general, the presence of microporosity increases the surface area, which likely leads to an increase in dissolution rate for the scaffold (16,95). This process may, in turn, lead to a faster and more uniform precipitation of biological apatite on the scaffold surface (15). If indeed the dissolution/precipitation process was the mechanism through which microporosity stimulated bone formation, assuming that the scaffold dissolved uniformly at the microscale level as suggested by Ducheyne's work (96), then the microenvironment within a MP scaffold and surrounding the MP rods would be uniformly conducive to bone formation. The biological apatite may have been present almost immediately throughout the scaffold following

implantation, providing an explanation for the relatively constant RBD and BF seen across time points in MP scaffolds.

2.4.4 Implications of the findings

This study has implications both in terms of the approach to the work and of the findings themselves. The results we obtained from the analysis are important in and of themselves and have not previously been shown, to our knowledge. The analysis of multiple measures of bone formation demonstrates that scaffold characteristics, such as microporosity, and treatments, such as BMP-2, that have been traditionally described as simply increasing bone volume, actually have separate and specific influences on the complex process of bone formation. Microporosity increased BF while BMP-2 increased SSA, and both resulted in more uniform distribution of bone throughout the scaffold. Thus, simply stating that the scaffold is "more osteoconductive" does not appear to be sufficient in comparing the efficacy of implanted scaffolds or scaffolds combined with biologics and/or cells; different components may serve different roles in the process. We also precisely defined “healing” and demonstrated that microporosity and BMP increase bone regeneration rate, or decrease healing time. A striking result was that healing time, as defined in Section 2.2.6.5, was at least two times faster in MP than in NMP in scaffolds and was at least four times in scaffolds with BMP than in scaffolds with No BMP.

Finally, our custom automated segmentation program, described in detail in Chapter 3, allowed for a 3-D characterization of large data sets (900 images/sample) for a large set of samples (100+), which is much more than other studies, to the best of our knowledge. Many studies have focused on only bone volume to compare efficacy of CaP scaffolds and most have used histologic methods, rather than micro-CT, to quantify bone formation. Such an approach provides very limited information. Our program made possible the analysis of multiple

measures of bone formation: volume fraction of bone, radial distribution, and specific surface area. Thus, the program enabled a more indepth and thorough assessment of bone formation in BCP scaffolds with periodic structure. Without it the analysis would be similar to other studies in the literature. The analytical process developed in this study can be applied to future studies, potentially setting a standard for scaffold evaluation after bone growth and allowing for more meaningful comparisons of scaffold performance across studies.

Microporous scaffolds and scaffolds with BMP reached steady-state for multiple measured outcomes. This is a strong indicator of rapid bone regeneration and healing. While a positive and encouraging outcome, it did not allow the process of bone regeneration to be observed. Larger scaffolds may allow for more discernable differences to be measured across time, which would give a more refined observation of bone formation, and potentially more interactions to be detected. We recognize that the dosage of BMP-2 is a parameter to control the response of the system to the growth factor, allowing this system to be sensitive to the delivery mechanism.

This study demonstrates different roles for microporosity and BMP in bone regeneration within BCP scaffolds and shows the potential of microporosity as an important parameter in scaffold design. However, in order to fully exploit this parameter, the mechanisms controlling bone regeneration in the presence of microporosity need to be established. We proposed mechanisms that may explain the measured effects. However, these mechanisms are not well-understood. A complete understanding of the process by which microporosity interacts with bone will be beneficial to designing scaffolds that accelerate healing and aid in the treatment of critical size defects. The knowledge gained in identifying and quantifying the different roles of microporosity and BMP adds a new dimension to rational scaffold design and analysis.

2.5 Conclusions

In this study we showed that microporosity and BMP-2 positively influence bone regeneration in BCP scaffolds in different, but perhaps complementary ways. Microporosity not only increased bone volume fraction, as others have also shown (21,31), but also improved the distribution of bone within the scaffold such that it was nearly perfectly uniform. In contrast, BMP-2 influenced specific surface area and bone distribution, which has not previously been demonstrated to our knowledge, but not bone volume fraction. Furthermore, both microporosity and BMP-2 accelerate healing, which we have defined using two criteria relating to steady-state bone volume and distribution (Section 2.2.6.5). Healing was at least twice as fast for BMP and MP samples as compared to NMP, and at least four times as fast compared to No BMP samples.

A custom micro-CT image segmentation program developed in our laboratory was used to make the most quantitative assessment of bone formation to date, to our knowledge. Use of the program elucidated the different roles of BMP-2 and microporosity in bone formation. Further, the program enabled a more sophisticated analysis in contrast to what is more typically seen for CaP scaffolds - histology and measures bone fraction only or bone fraction and bone apposition..

In order to fully exploit the positive effects of microporosity on bone regeneration, the mechanisms must be established. The mechanisms we describe are not yet well-understood. A complete understanding of the interaction between microporosity and bone may lead to scaffold designs that significantly accelerate healing and aid in critical size bone defect repair, one of the remaining barriers to tissue engineering.

Chapter 3. Segmentation Algorithm

3.1 Introduction

In order to fully utilize the data available from the micro-CT images in the *in vivo* study, pixel-by-pixel segmentation was necessary. Due to the nearly identical mineral composition of hydroxyapatite and bone, much overlap existed between the two materials' grayscale values. The amount of overlap varied between scaffolds and time points, and a set threshold value for segmentation was difficult to estimate and thus unreliable. Manual segmentation was not feasible owing to the potential for subjectivity, the time required to segment each image (3-4 hours), the large number of images to be segmented (900 images per sample), and the number of samples to be analyzed (+100). Therefore a custom segmentation algorithm was needed. The custom, automated software that was developed makes use of a combination of grayscale values, the periodicity of the scaffold, and 3D spatial relationships between bone and scaffold, to achieve segmentation. The time required for segmentation of one sample was approximately one hour, a 900-fold improvement over manual segmentation.

3.2 Region of Interest and Orientation Identification

3.2.1 Region Identification

The halo region discussed in Chapter 2.2.6.2 was identified and removed from the pre-processed images using a user specified threshold value, leaving only the region of interest (ROI). Noise from the scan caused pixels outside the scaffold, in the halo region, to have grayscale values greater than zero thus necessitating the user-specified threshold value (Fig. 3.2b). Once thresholded, each image was scanned pixel by pixel four times, scanning from each corner horizontally and vertically moving towards the center (Fig. 3.1). In each of the four scans, pixels initially identified as outside the ROI, remained outside only if the adjacent and already scanned pixels were also labeled as outside the ROI. If one adjacent pixel was labeled inside the

ROI and the other adjacent pixel was outside the ROI, the pixel in question would remain in the ROI (Fig. 3.1a). If both adjacent pixels were identified as in the ROI, then the pixel in question would remain in the ROI (Fig. 3.1b). However, if both adjacent pixels were considered outside the ROI, the pixel in question would be outside the ROI as well (Fig. 3.1c). This step was done for each image in the stack to create a mask, or image map with the ROI data.

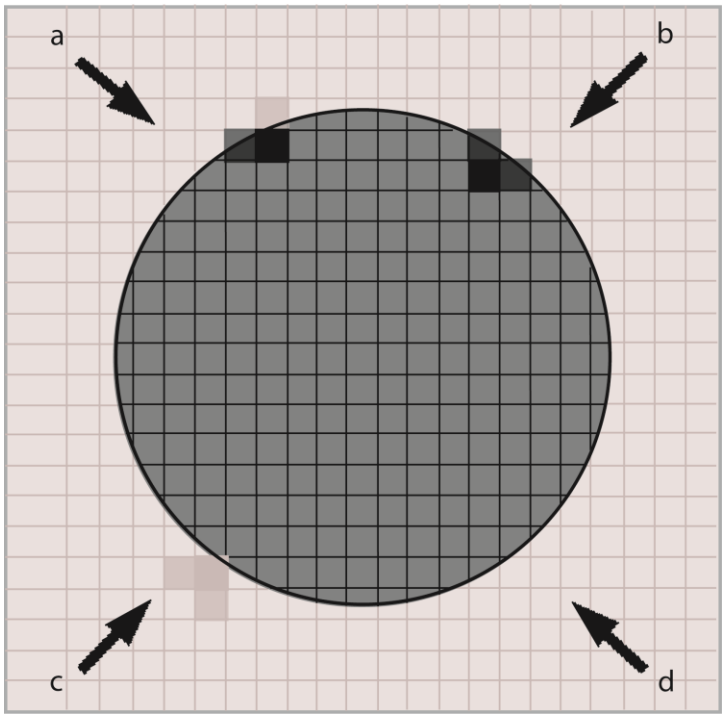

Figure 3.1. Schematic of region identification. The three clusters of highlighted pixels represent possible scenarios. (a), (b), and (c) indicate different possible decisions in cropping and each arrow represents a different image scanning direction.

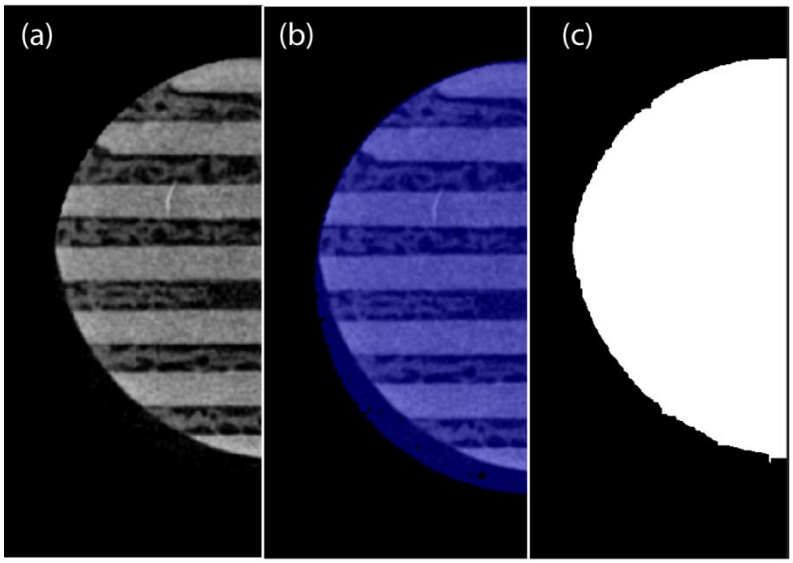

Figure 3.2. Region identification for representative sample. (a) Micro-CT image of half the circular sample. **(b)** Simple thresholding identifying in blue all pixels with grayscale values of 1 or greater. **(c)** After cropping, the region in white was deemed the region of interest for the segmentation program.

3.2.2 Thresholding the background

Thresholding was used to first identify the background, which included fluid and soft tissue. Simple automated thresholding was used here because the attenutation of the background was sufficiently different from both scaffold and bone. The automated thresholding minimzed the within group variance between background (fluid and soft tissue) and foreground (bone and scaffold). A histogram of the image was generated and the probability of occurrence for each grayscale value was calculated. A cumulative probability density was determined for every grayscale value in the histogram, above and below the test threshold value (Eqn. 3a and 3b). The most likely grayscale value was then determined in each group (Eqn. 4a and 4b), the groups being either grayscale values greater than or equal to the test threshold value or grayscale values less than the test threshold value. Variance was then summed for each group (Eqn. 5a and 5b) and the process repeated until the grouping with the smallest variance was

found (Eqn. 6). The threshold value for each image was stored and used as a feature (1.6.2) for segmentation later in the algorithm (3.5). In the algorithm, the initial grayscale value (z) and the most likely grayscale values (u_0 and u_1) were set to zero. The program iterated through all possible test threshold values and these variables were updated until optimized (Appendix A.4 *autothresh*).

$$q_0 = \sum_1^{z_{t-1}} \Pr(z) \quad (3a)$$

$$q_1 = \sum_{z_t}^{z_f} \Pr(z) \quad (3b)$$

Where z_t = test threshold value
q_0 = the cumulative probability of a grayscale value less than z_t
q_1 = the cumulative probability of a grayscale value z_t or greater
Pr = probability

$$u_0 = u_0 + z \cdot \Pr(z)/q_0 \quad (4a)$$

$$u_1 = u_1 + z \cdot \Pr(z)/q_1 \quad (4b)$$

Where u_0 = the most likely grayscale value less than z_t
u_1 = the most likely grayscale value greater than or equal to z_t

$$o_0 = o_0 + (z - u_0)^2 \cdot \Pr(z)/q_0 \quad (5a)$$

$$o_1 = o_1 + (z - u_1)^2 \cdot \Pr(z)/q_1 \quad (5b)$$

Where o_0 = the sum of the variance of values less than z_t
o_1 = the sum of the variance of values greater than or equal to z_t

$$o_w = q_0 \cdot o_0 + q_1 \cdot o_1 \quad (6)$$

Where o_w = the within group variance

3.2.3 Orientation identification

The orientation of the scaffold rods in each image – i.e. vertical rods, horizontal rods, or orthogonal rods – was then determined in order to aid in differentiating and segmenting the scaffold and bone (3.3.1). A correlation filter was employed for this purpose (Eqn. 7).

$$(f * g)x = \int_{-\infty}^{\infty} f^*(\psi)g(x+\psi)d\psi \qquad (7)$$

Where
f = image matrix
g = window
x = position vector
ψ = position lag vector

Two filter window shapes, 100x1 and 1x100, were used for each image to emphasize vertical and horizontal rods, respectively (Fig. 3.3a and 3.3d). The grayscale values in the resulting images (Fig. 3.3b and 3.3e) were then summed along columns or rows of pixels. The grayscale values of the image that resulted from the 1x100 window (Fig. 3.3e) were summed along columns (Fig. 3.3f) and the grayscale values of the image that resulted from the 100x1 window (Fig. 3.3b) were summed along rows (Fig.3.3c). The average value for each column or row was found. Next, a histogram was generated for all non-zero average values and the same thresholding procedure as described in Section 3.2.2 was performed. All values greater than or equal to the threshold were assigned a value of one and the remaining values assigned zero. The resulting vector was used to identify rods and the spaces between the rods (Fig. 3.3c and 3.3f). If the number of transitions between rods and the space between rods was greater than two for one of the filtered images (Fig. 3.3f), the orientation of the window was parallel with the orientation of the scaffold rods. A number of transitions of two or less (Fig. 3.3c) indicated that only the edges on the scaffold were identified and the orientation of the window was not aligned with the orientation of the scaffold rods. If both images had greater than two transitions, the image was deemed an orthogonal section where horizontal and vertical scaffold rods were both present.

The binary orientation variables for each image, scaffhor and scaffver, were each assigned a value based on result of the analysis. If the image had only horizontal rods, scaffhor was set as one and scaffver was zero. Scaffhor was zero and scaffver was one if the image had only vertical rods. If the image had orthogonal rods, both scaffhor and scaffver were recorded with a value of one. These variable values were saved for later use as features (Section 3.4).

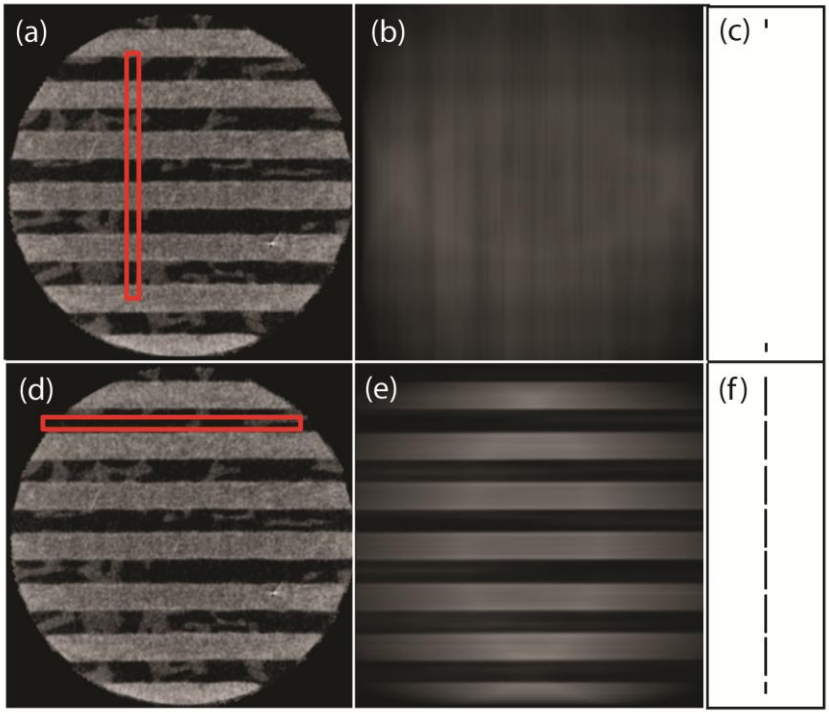

Figure 3.3. Orientation identification. (a) A horizontal orientation image with a vertical correlation window resulted in **(b)**. The row averaging and identification of transitions **(c)** determined that this image was not a vertical orientation image. **(d)** The same image as **(a)**, but with a horizontal correlation window resulted in **(e)**. The row averaging and identifications of transition **(f)** determined that this image was a horizontal orientation image.

3.3 Initial Labeling

3.3.1 Use of scaffold geometry - application of correlation

Once the orientation of each image was determined a correlation filter was used to take advantage of the geometry of the scaffold rods in segmenting scaffold from bone. A correlation filter with a 10 x 10 pixel window was applied to identify the edges of the scaffold rods (Fig.

3.4b). Row and/or column averages were taken, depending on the orientation decision made in Section 3.2.3. A histogram was made using the row/column averages and a threshold value was identified using the same autothresholding algorithm described previously (3.2.2). If the orientation was identified as orthogonal, threshold values for both rows and columns were taken and the average value used for segmentation. The threshold values for each orientation (ztscaff_ver and ztscaff_hor) was stored for use later in the algorithm (3.4).

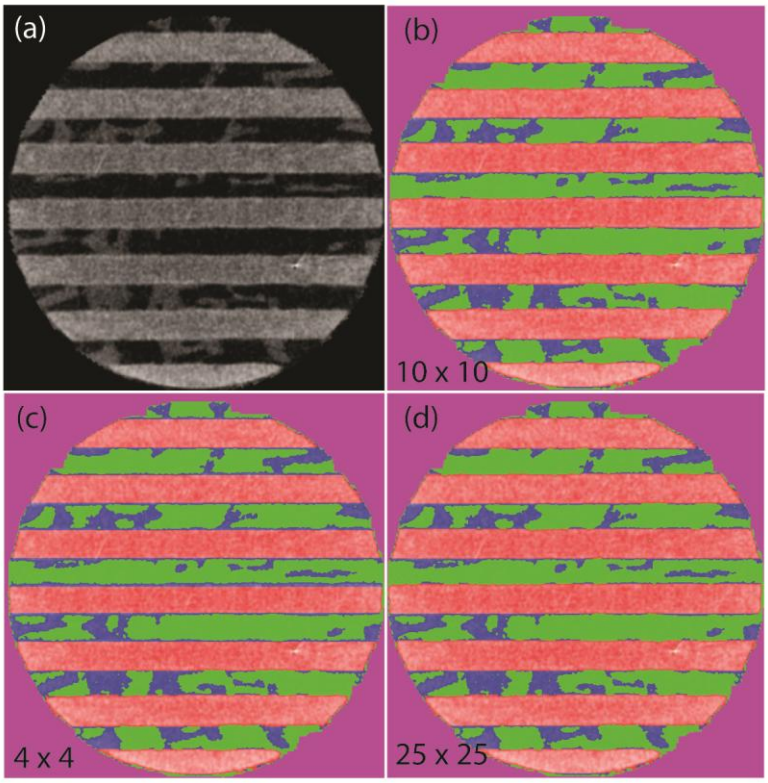

Figure 3.4. Effect of the window size of the correlation filter. (a) Micro-CT image of a CaP scaffold with bone ingrowth. **(b)** Segmentation of the image in **(a)** with a 10x10 correlation window. Green is background, blue is bone, and pink/orange is the scaffold. **(c)** and **(d)** are segmented images of **(a)** with different correlation filter sizes. **(c)** has a 4x4 window which results in small diameter rods and over estimation of bone. **(d)** has a 25x25 window which, while similar to the 10x10 window, results in larger diameter scaffold rods for scaffolds with poorer quality scans.

3.3.2 Optimization of correlation filter

Several parameters used in the automatic segmentation were optimized through manual iteration. The window size of the correlation was one such parameter. The 10x10 pixel window was selected such that the segmentation values between manual and automatic were as similar as possible (Fig. 3.4b). This value was determined via manual optimization. Scaffold material was used for optimization as the correlation had a clear effect on that material. Twenty images were labeled manually and the scaffold pixels of each of those images were compared to automatic segmentation using paired t-tests. This was repeated for automatic segmentation using different correlation windows (Fig. 3.5). The window was initially set at 35x35, however the automatic segmentation over-labeled scaffold by 2642 voxels, approximately 3%. While this was not significant ($p=0.11$), error could be further reduced. At a window size of 15x15 there was also no significant difference between manual and automatic segmentation, though the average scaffold pixel count was nearly 1000 pixels larger than the manual count (Fig. 3.5). At a size of 10x10 there was no significant difference between manual and automatic segmentation ($p=0.86$), and the difference in pixel labels between the two methods was 180, approximately 0.2%. The next smaller correlation window tested was 4x4. While there was still no significant difference between manual and automatic segmentation ($p=0.44$), the number of different pixels increased to 757, or approximately 0.8%.

The standard error between the images for manual segmentation was ± 1306 (1.4%) and the standard error between the images for the 10x10 window was ± 1628 (1.7%). This error in manual segmentation is expected as each image had a different scaffold orientation - vertical/horizontal, cross-hatched, and transitional – and contained different amounts of scaffold. Thus a standard error in automatic segmentation near that of the manual segmentation indicated good fidelity across a range of image types.

Visual inspection also aided in window selection, with the most striking results seen with smaller windows. Shown in Fig. 3.4, the smallest window, 4x4, produced narrow scaffold rods with bone directly apposed to most of the scaffold rods with almost uniform thickness (Fig. 3.4c). The micro-CT image (Fig. 3.4a) showed that bone was clearly not coating the scaffold rods as the small window suggested. In considering the number of identified scaffold pixels, the standard errors, and visual inspection, the 10x10 window was deemed optimum.

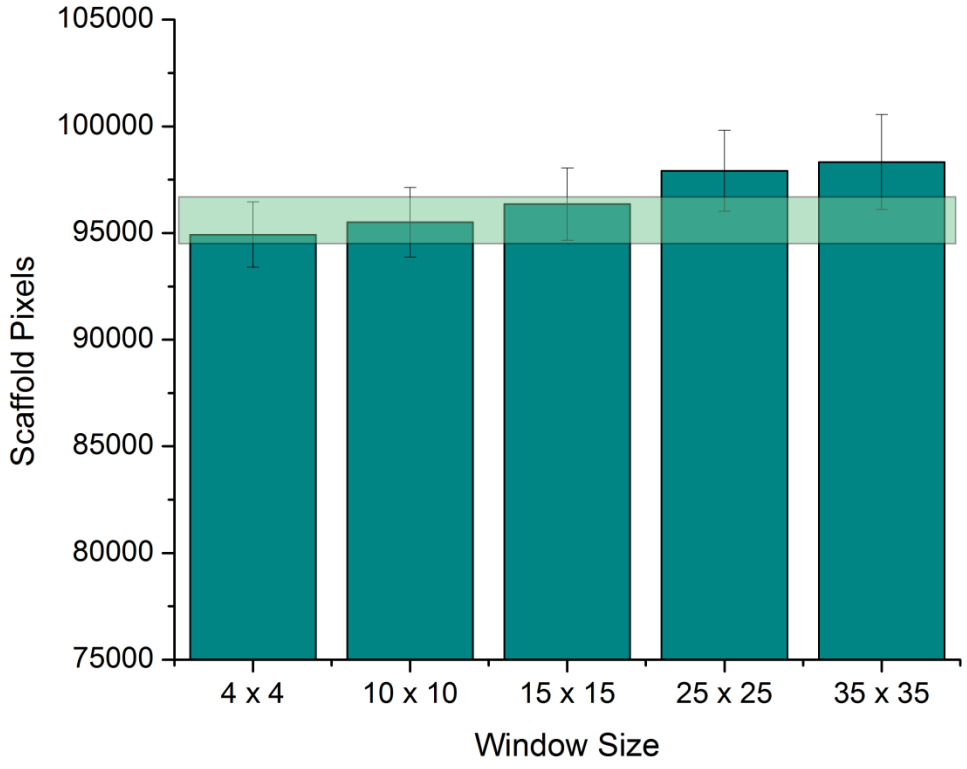

Figure 3.5. Effect of the window size of the correlation filter on scaffold labeling. The pale green box is defined by the average and standard error of manual scaffold labeling. The 15 x 15, 10x10, and 4x4 windows for automatic segmentation most closely match with the manual segmentation, however the 10x10 window is the better match as the pixel average and standard error is nearly identical to manual segmentation. N=20

3.3.3 Application of Hysteresis

As bone at different states of mineralization attenuates differently even within the same sample, hysteresis was used to detect the bone/background borders within the scaffold macropores. Hysteresis is a gradient or edge detection method that uses two threshold conditions. The first threshold is more stringent, but could mislabel some regions. In the second iteration, a less stringent threshold is used in conjunction with additional labeling criteria such as the spatial relationship of the materials. In this algorithm hysteresis was used to improve segmentation of the bone/background interface. Initial segmentation was done using the higher of the two thresholds and followed by recursive segmentation on neighboring pixels using the lower threshold.

Prior to the application of the hysteresis algorithm, all pixel grayscale values above the background threshold (ztback) from Section 3.2.2 were selected. These pixels were either bone or scaffold. If the pixel grayscale value was above the scaffold threshold (ztscaff_hor or ztscaff_ver) from Section 3.3.1., the pixel was labeled as the higher attenuating material of the two, the scaffold. Else the pixel was labeled as bone. All pixels with grayscale values less than the background threshold were labeled as background.

Next, the hysteresis step was applied. Pixels with a grayscale value greater than two-thirds of the background threshold that were also immediately adjacent to a pixel labeled as bone were relabeled as bone. If the pixel was not adjacent to bone it remained background (Fig. 3.6b). The labeled image as well as the grayscale image were saved and used in the next step of segmentation.

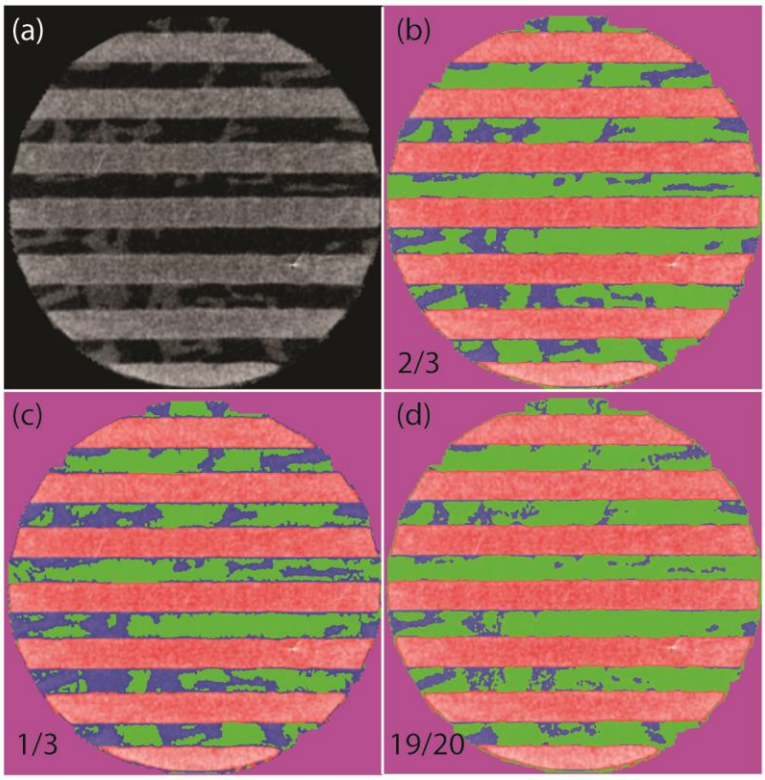

Figure 3.6. Effect of hysteresis threshold value. (a) An unsegmented micro-CT image of a CaP scaffold with bone ingrowth. **(b)** is the image in **(a)** segmented using a relaxed threshold for pixels adjacent to bone, the value is 2/3 the initial threshold. Segmentation colors have the same assignments as described in Fig. 4. **(c)** and **(d)** are segmented images using relaxed threshold values of **(c)** 1/3 the original value and **(d)** 19/20 the original value. Inspection reveals the 2/3 value to most accurately segment bone.

3.3.4 Optimization of hysteresis threshold

The hysteresis threshold (h) was optimized using a similar procedure as correlation window size (3.3.2). Values between one-third and 19/20 were tested on twenty images (Fig. 3.6) and compared to the manual segmentation of bone for those same images using paired t-tests (Fig. 3.7). The hysteresis value of two-thirds was the only value tested that resulted in segmentation of bone that was not statistically different from the manual segmentation ($p=7.7E-13$, $h=1/3$; $p=1.06E-4$, $h=1/2$; $p=0.37$ $h=2/3$; $p=7.3E-6$ $h=3/4$; $p=2.9E-14$, $h=19/20$). Bone pixels for the automatic segmentation were only 789 fewer in the automatic than in the manual

(2.7%). The value h=1/3 resulted in the most difference between manual and automatic segmentation with 67% more bone pixels than the manual segmentation. The implications of these statistics can be seen in Fig. 3.6. The highest threshold value (Fig. 3.6d) shows additional bone fill unlike what is seen in the micro-CT image (Fig. 3.6a). In contrast, the low threshold (Fig. 3.6c) shows far more bone than in the micro-CT image (Fig. 3.6a), especially in the upper right region of the image. Thus, visually and statistically, two-thirds was the optimum hysteresis threshold.

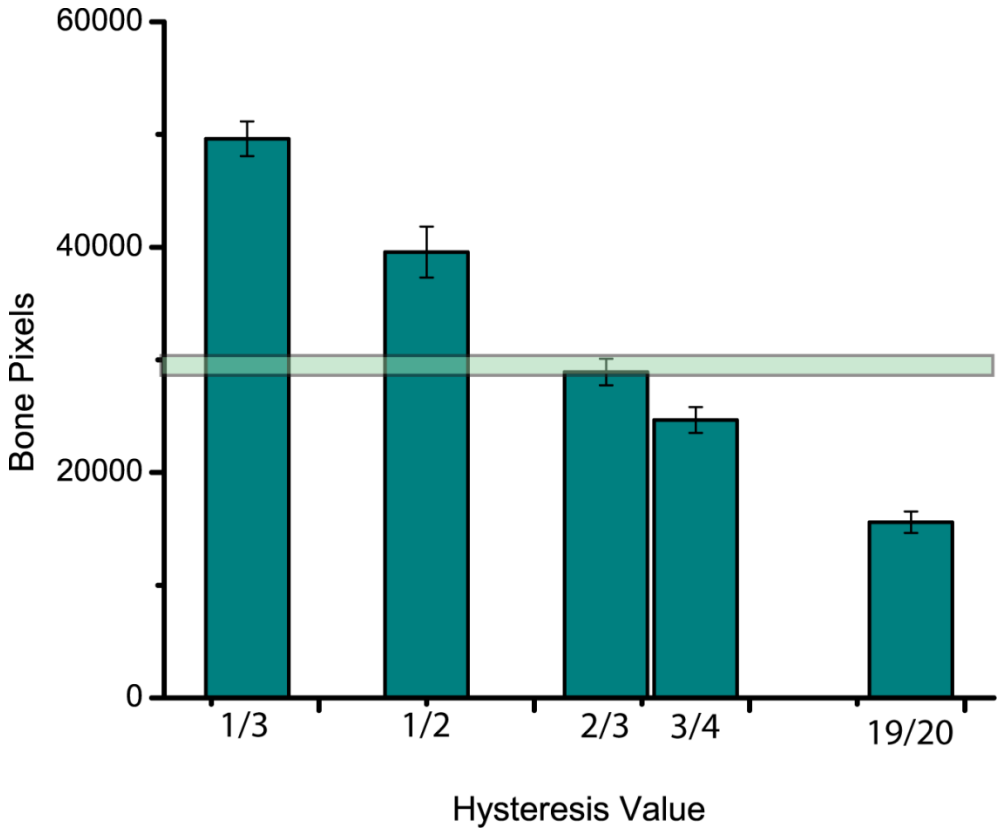

Figure 3.7. Effect of hysteresis value on bone segmentation. All hysteresis values except 2/3 resulted in bone segmentation that was statistically different than manual segmentation (p=7.7E-13, h=1/3; p=1.06E-4, h=1.2; p=0.37 h=2/3; p=7.3E-6 h=3/4; p=2.9E-14, h=19/20). The pale green box is defined by the manual segmentation bone values and the associated standard error. N=20

3.4 Modified Classifying/Artificial Neural Networking

An appropriate program for automated classifying or artificial neural networking (ANN) could not be found to accommodate the size of the desired training set and capture the complexity of three material segmentation and spatial relationships. Thus a modified classifying (1.6.2) approach was used. Training sets were created and potential features of importance were identified and weighted using the skills and intuition developed from manual segmentation and studying histology samples. A decision network was then created that used the periodicity of the scaffold to improve segmentation accuracy. The features used were highlighted in previous sections as saved values. This included: background threshold (ztback), horizontal window threshold (ztscaff_hor), vertical window threshold (ztscaff_ver), the binary horizontal orientation (scaffhor), the binary vertical orientation (scaffver), the image labels from Section 3.3.3, and the original grayscale image. These features, along with the same set of features two images above and below the image, were collected for a total of 5 sets of image features.

Due to the scaffold geometry and periodicity, images containing orthogonal scaffold rods occurred regularly in every scaffold as did images with the top and bottom edges of scaffold rods. Images containing the orthogonal rods were segmented properly by the previously discussed algorithms. However, images in the sample stack immediately above and below the orthogonal rod images were not. These “transition” images were characterized by faint or low intensity pixels as one layer of scaffold rods faded out and another layer faded in. The low intensity scaffold pixels were typically labeled as bone by the algorithm, thus additional steps were required for accurate segmentation. As the image stack was always read from the top of the scaffold to the bottom, the identification of the very top and bottom images of a scaffold rod – in the transition images – was improved following the procedures outlined below.

Identifying the top and bottom images of a scaffold rod required similar steps, the only changes were due to the order in which scaffold was expected when scanning in a constant direction. In the case of segmenting the top image of a scaffold rod, a positive scaffold pixel gradient was expected, i.e. the number of scaffold pixels increase as the program progresses through the image stack. To quantify the gradient, the scaffold fraction of the image below was subtracted from the scaffold fraction of the above image. If that difference was large, greater than 15%, and the images one and two below had a high scaffold fraction, the image in question was deemed to be at the top of a scaffold rod (Fig. 3.8a). If the image had a larger bone fraction, the scaffold in the image was mislabeled as bone (Fig. 3.8d) and the pixels re-segmented as scaffold (Fig. 3.8g). A negative scaffold pixel gradient was expected when segmenting the bottom image of a scaffold rod, i.e. a greater scaffold fraction *above* the image than below the image was expected. The two images *above* needed a large scaffold fraction, and, as before, the image in question needed a large bone fraction. If those requirements were met, the image was identified as at the bottom of a scaffold rod and bone in that image was deemed mislabeled.

The final improvement in the segmentation utilized the structure of the scaffold and the physical limitations on bone growth. Due to the design of the scaffolds, scaffold pixels must be adjacent to at least one other scaffold pixel. Therefore if a pixel was labeled as scaffold (Fig. 3.8e and 3.8f), but neither the pixel above nor below was scaffold, then the pixel in question was relabeled as a bone pixel (Fig. 3.8h and 3.8i). These improvements were applicable to images with small (10 µm) and large (17 µm) voxel sizes as well in images with different fractions of bone fill (Fig. 3.8b and 3.8c).

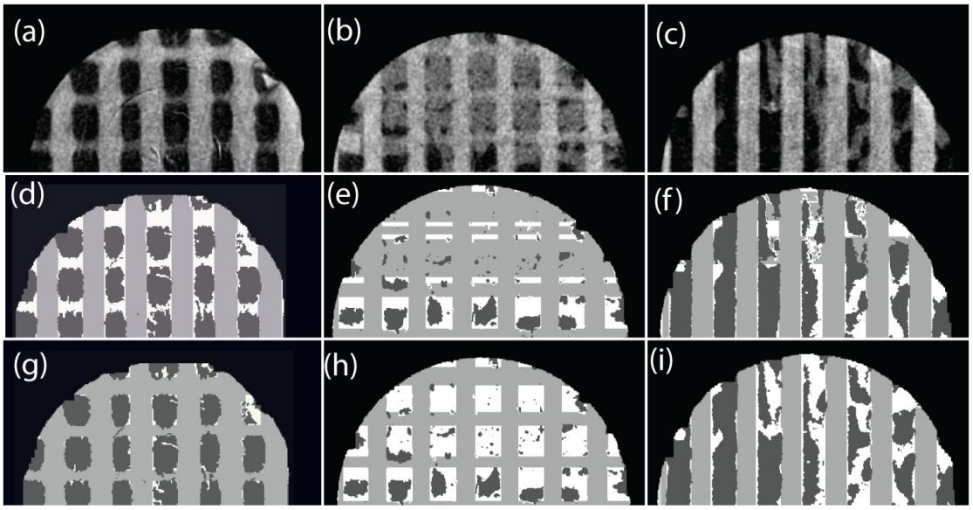

Figure 3.8. Application of modified classifying. (a)-(c) Representative micro-CT images. **(a)** A high quality image (voxel size 10 µm) of region of scaffold with strong vertical scaffold rods and faint horizontal scaffold rods. **(b)** A lower quality image (voxel size 17 µm) with a high fraction of bone fill. **(c)** A typical high quality image. **(d)-(f)** Segmentation using the thresholding and hysteresis, before the modified classifier segmentation. Note in **(d)** the mislabeled scaffold rods, in **(e)** the labeling of bone as scaffold, and in **(f)** the addition of scaffold where scaffold cannot be located. **(g)-(i)** After the spatial segmentation. **(g)** Faint scaffold rods are correctly labeled. **(h)** Appropriate scaffold pattern identified. **(i)** Mislabeled scaffold regions now correctly identified as bone.

3.5 Evaluation of performance: manual vs. automatic segmentation

Three representative scaffolds from the *in vivo* study were selected evaluate the performance of the automatic segmentation program as compared to manual segmentation for randomly selected images in those scaffolds. The *in* vivo study used two different voxel sizes, 10 µm and 17 µm, depending on the size of the sample being imaged. As the higher resolution scans were more common, two of the scaffold data sets selected had high resolution and one scaffold data set had low resolution.

An additional scaffold data set was selected to measure the performance of the automatic program for difficult to segment (DTS) images. DTS images have characteristics such as low attenuating scaffold rods in transition images (section 3.4) and missing sections of the scaffold. While the images selected from the scaffolds described in the previous paragraph

were random and did include some DTS images, the DTS accuracy was determined independently in order to represent a worst case value. Therefore transition images from a scaffold with minor damage caused by implantation and retrieval were chosen for this purpose. The images from the fourth "damaged" scaffold were not used in the overall comparison of manual and automatic segmentation. Instead, images from the fourth sample were evaluated separately for the assessment of "worst case scenario".

3.5.1 Average accuracy of segmentation program

The average accuracy of the three-material automatic segmentation was assessed by summing the differences between manual and automatic segmentation for each material in randomly selected images from the three representative scaffolds described above. Paired t-tests were used to evaluate statistical similarity. The standard error for the overall accuracy was calculated accounting for propagation of errors using the square root of the sum of the squares of the error for each material (Eqn. 8a and 8b)[1].

$$z = a + b + c \tag{8a}$$

$$\Delta z = \sqrt{\left(\frac{\partial z}{\partial a}\right)^2 (\Delta a)^2 + \left(\frac{\partial z}{\partial b}\right)^2 (\Delta b)^2 + \left(\frac{\partial z}{\partial c}\right)^2 (\Delta c)^2} \tag{8b}$$

Where
a, b, and c = measured values
Δa, Δb, and Δc = error associated with measure values
z = sum of measured values
Δz = error associated with the summed term

[1] Multiple errors arose as three materials were segmented and each material had an associated error.

The automatic program had an accuracy of 94.2% ± 3.3% and no statistically significant difference was found between any material when comparing the fractions of each material obtained using manual and automatic segmentation (Fig. 3.9). Manual segmentation resulted in a background fraction of 0.295 ± 0.012, a scaffold fraction of 0.557 ± 0.011, and a bone fraction of 0.149 ± 0.011. The automatic segmentation of the same images measured background at 0.265 ± 0.014, scaffold at 0.565 ± 0.016, and bone at 0.170 ± 0.016.

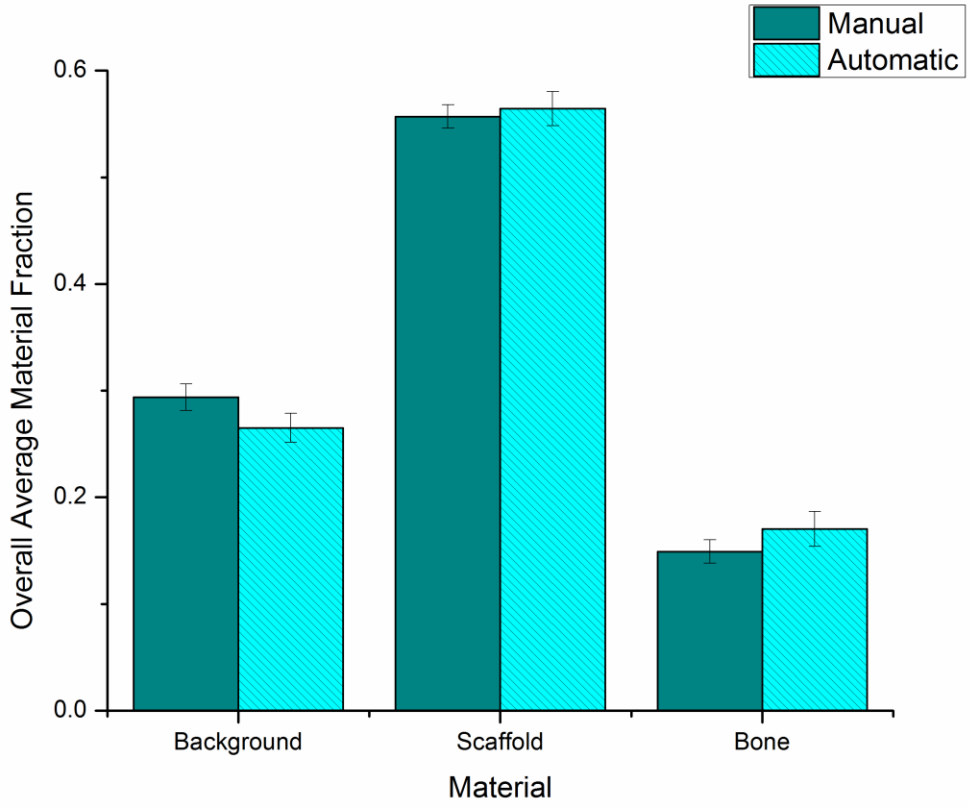

Figure 3.9. Manual versus automatic segmentation of randomly selected images. There was no significant difference between manual and automatic segmentation of any of the three materials (Background p=0.128, Scaffold p=0.699, Bone p=0.289).

Evaluation of DTS images using Eqns. 8a and 8b resulted in an accuracy of 80.41% ± 2.24%. Nineteen DTS images were selected and each segmented manually by three to four independent researchers as well as by the automatic program. Fractions of Background, Scaffold, and Bone were all found to be statistically different between the manual and automatic segmentation for the DTS images (p=6.02E-9, p=0.0203, p=6.35E-6) (Fig. 3.10). Manual segmentation of the sample's DTS images resulted in a background fraction of 0.352 ± 0.010, a scaffold fraction of 0.560 ± 0.006, and a bone fraction of 0.089 ± 0.007. Automatic segmentation of the same sample images identified the background to be 0.25426 ± 0.009, the scaffold to be 0.59263 ± 0.01184, and the bone to be 0.153 ± 0.010.

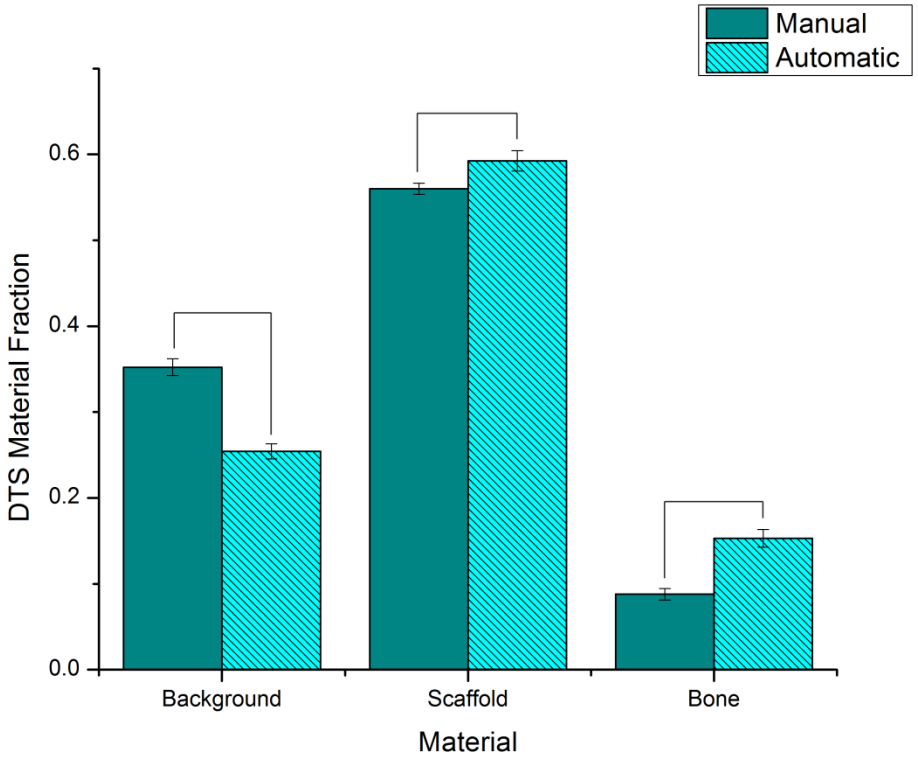

Figure 3.10. Manual versus automatic segmentation of DTS images. Automatic segmentation underestimates background pixels (p=6.02E-9) and over estimates bone pixels (p=6.35E-6). Scaffold pixels are slightly over identified in automatic segmentation (p=0.0203).

3.5.2 Pixel-by-pixel segmentation accuracy

A pixel-by-pixel position comparison between manual and automatic segmentation was performed using the same method to account for propagation of error as described in 3.5.1. and resulted in an accuracy of 88.2% ± 9.5%. The overall analysis of the segmentation discussed in 3.5.1 did not take into account how compensating errors affected the overall accuracy. For example, if 500 bone pixels were labeled as scaffold, but 400 scaffold pixels were labeled as bone, the overall accuracy assessment would only consider 100 pixels mislabeled. The pixel by pixel analysis compared the labeling of pixel in location (i,j) of the manually labeled image to the labeling of pixel (i,j) in the automatically labeled image. Random images were selected from the three representative samples to create a confusion matrix of errors (Table 3.1). This table shows the fraction of identically labeled pixels between manual and automatic segmentation along the diagonal. The remaining cells of the table show where the labeling errors occurred. Each row sums to the fraction manual segmentation assigned to each material and each column sums to the fraction automatic segmentation assigned to each material. For example, the value 0.010 in row one, column two of Table 3.1 states that 1% of the total pixels in the image were assigned to background by the manual segmentation and to scaffold by the automatic segmentation. This method of data representation has been used in segmentation of brain MRI images, but has not been used in scaffolds or, to our knowledge, in micro-CT images. The use of a confusion matrix is important in understanding common errors and can be of assistance both in interpreting material fraction results as well as in improving the segmentation algorithm.

A plot of standard deviation versus number of samples (N) was used to determine how many images were required for a proper sample size (Fig. 3.11). The standard deviation likely increased around the seventh image as that image was a DTS. However, the standard deviation of each measured error plateaued by N=11.

Table 3.1. Confusion Matrix for Sample Accuracy

Values in each cell contain the fraction of pixels labeled by automatic and manual segmentation. Cells along the diagonal contain the fractions of pixels labeled with the same material.

		Automatic		
		Background	Scaffold	Bone
Manual	Background	0.243	0.010	0.016
	Scaffold	0.005	0.516	0.055
	Bone	0.010	0.022	0.122

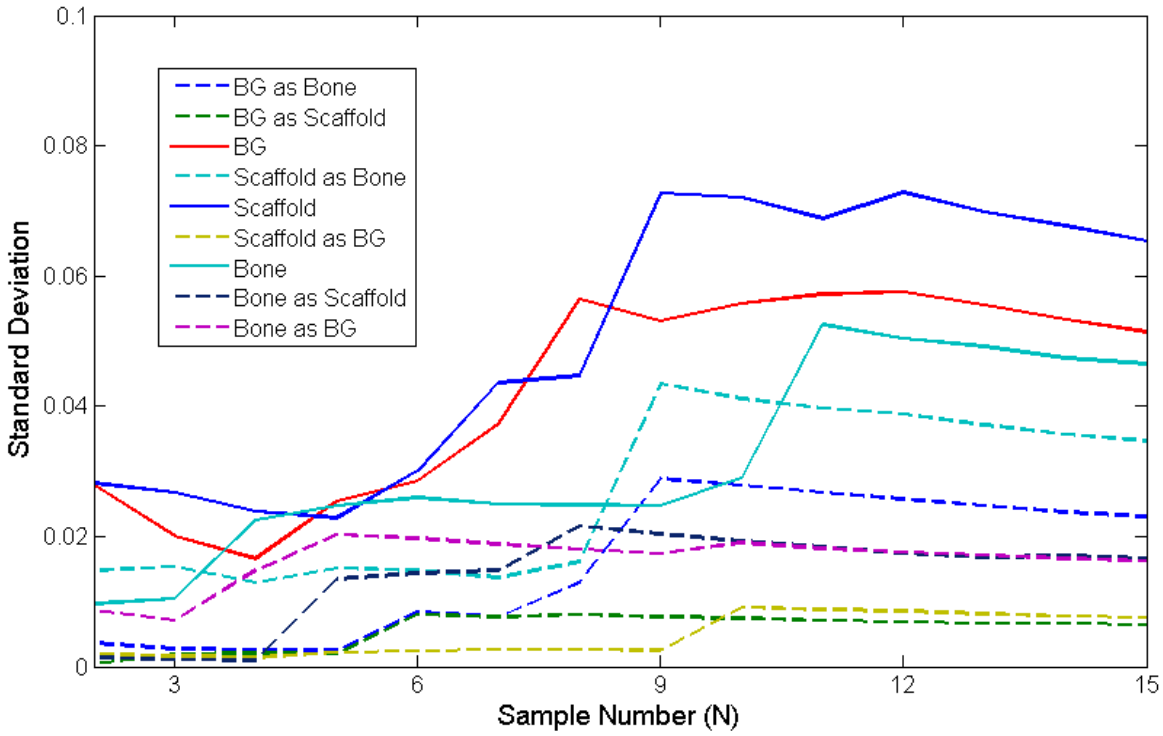

Figure 3.11. Standard deviation versus sample number. After 11 images the standard deviation for each possible labeling outcome plateaus indicating that an appropriate sample size has been reached and additional images will not improve the standard deviation. "BG" in the legend refers to Background and the first material listed in each legend description is the material assignment from manual segmentation, the second material listed is the material assignment from the automatic segmentation.

Manual segmentation of some of the very poor quality images was inconsistent, thus comparison of the automatic segmentation to manual segmentation would not have yielded meaningful results. Images shown in Fig. 3.12a, 3.12c, and 3.12e provide examples of such micro-CT images. Fig. 3.12a and 3.12c are images from histology samples and 3.12e is an image with 17 μm voxels. These samples were most likely segmented by the automatic program with a bias towards bone as the low resolution and contrast "blurred" the image and increased the number of pixels that fall along the Background/Bone and Bone/Scaffold transition grayscale regions. However, automatic segmentation was deemed adequate as it was objective, logical, and consistent in labeling, thus allowing for comparison of material fractions even with less than ideal sample images.

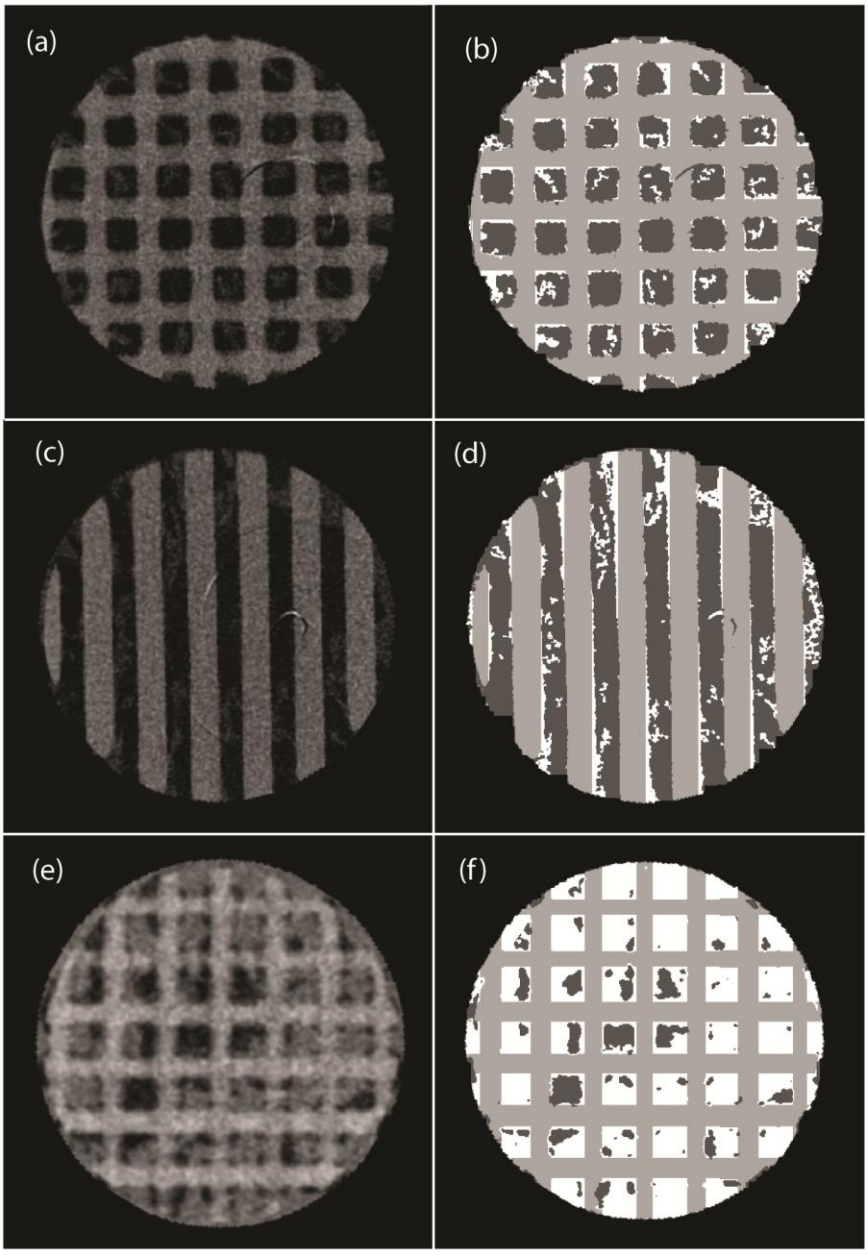

Figure 3.12. Segmentation of lower quality micro-CT scans. (a) and **(c)** are images from histology samples scanned at 10 µm with 1048 x 2000 pixels per image. Note the small grayscale values of the bone and scaffold. **(b)** and **(d)** are the corresponding automatic segmentations. **(e)** is a micro-CT scan of a non-histology scan at 17 µm with 524 x 1000 pixels per image. Note the nearly identical grayscale values of bone and scaffold. **(f)** is the corresponding automatic segmentation.

3.6 Discussion of the Automatic Segmentation

In this work we developed a custom, automated segmentation program to analyze the fraction of materials (bone, scaffold, and background/soft tissue) in 900-image data sets of CaP bone scaffolds, obtained using micro-CT. The similarity in attenuation between scaffold and bone makes segmentation in this system particularly challenging. However, the program developed has the capability to differentiate these two materials, plus the background/soft tissue, with an average accuracy of 94.2% ± 3.3%. Further, the volume fractions of the three materials calculated using the program were statistically similar to those obtained using manual segmentation. The level of accuracy is impressive as it accounted for scans with different resolutions, images in different locations within each sample, images in different samples, and variations in bone volume from image to image. Segmentation of two materials, which is considered to be a much simpler task, typically shows a level of accuracy of 90% or less for micro-CT images (97-99). Several studies have developed automatic segmentation programs for micro-CT images of CaP scaffolds. However, scaffolds were either not implanted, so only two materials had to be segmented (67,70) or the program was not validated (71). The segmentation in the former case, with only two materials, was done by atlas mapping or thresholding (1.6.3). In the latter cases, the volume fraction of bone determined by the program had a statistically different fraction than the validation method (69) or no validation method was described (71). Thus, the program developed here is a marked improvement to what is already in the literature.

A pixel-by-pixel analysis was done that compared pixels at position (i,j) labeled manually to pixels (i,j) labeled with the program. The pixel-by-pixel position accuracy was 88.2% ± 9.5%, which is similar in magnitude to values reported by others for the overall average accuracy, that does not take account position, and that only has two materials (97-99).

Segmenting three materials and performing the associated error analysis presents a number of challenges. In two material segmentation, pixels are separated into either background or foreground. Grayscale values for two materials can be more easily distinguished as the grayscale range only contains two materials. In a three material segmentation the range of grayscale values is shared by three different materials, which are more likely to have overlapping attenuations. Additionally, error analysis is more straightforward when only two materials are present; the category of a mislabeled pixel is immediately known. Error analysis was complicated here by three materials as a mislabeled pixel may have been categorized as one of two incorrect materials (Table 3.1).

Our data had a range in quality of the images and, while these images made segmentation more challenging, the program segmented the images with a high level of accuarcy. The lower quality images were from samples that had a larger diameter. These samples were designated for histology and were therefore excised with a ring of bone surrounding the scaffold. This resulted in a degradation of image quality from two sources. The first is that the pixel size had to be larger. While the smallest possible size was used (2.2.6.1), the pixel size was limited by the field of view and larger samples required a larger field of view. The second source of lesser image quality was the additional mass that the incident x-rays had to penetrate, which reduced contrast in the images. Approximately one-third of the samples imaged fell into the category of lower quality images.

The automatic segmentation program required some manual pre-processing prior to implementation of the segmentation algorithm. Such steps included image filtering, removal of the bone ring, and aligning the scaffold rods with the global coordinate system (2.2.6.2). The alignment was the most time consuming manual step, but this step could potentially be eliminated with the implementation of a Hough transform, which is an edge detection algorithm

that uses a voting system to determine where the most likely locations are for lines in an image (100). Various algorithms such as the watershed algorithm, which is a region growth method that segments based on local maxima in grayscale vales (1.6.2), in addition to computer learning may improve segmentation of DTS images.

3.7 Conclusions

In this chapter, we demonstrated that the automatic segmentation program developed was exceptionally accurate with an average accuracy of 94.2% ± 3.3%. There are no other relevant comparisons in the literature for the segmentation of three materials in bone scaffolds. However, the accuracy shown here is the same of better than accuracies shown from MRI imaging using atlas based three-material segmentation of cerebral hemispheres. Additionally, the volume fractions of each of the materials (bone, scaffold, and background) determined using the segmentation algorithm were statistically similar to those determined from manually segmented images. The subset of images used in the error analysis included images with larger voxels, or poorer quality images, as well as images with different levels of bone fill and images from different locations in the scaffold. The automatic segmentation program was also much faster than manual segmentation; the program takes approximately one hour to segment 900 images, while a single image takes one hour using the manual method.

This automatic segmentation program is unique in its capabilities; while there have been attempts at automatically segmenting micro-CT images of CaP bone scaffolds, to our knowledge no successfully validated three material method currently exists. An algorithm for segmenting and comparing CaP scaffolds using micro-CT has been developed, but it does not segment bone fraction; it has been used only on empty, non-implanted scaffolds (67,70). A three material segmentation method for CaP scaffolds was developed, however when compared to SEM images, the bone fraction measured by the automatic program is statistically different (69).

While the automatic segmentation program presented here was designed at optimized for the images in this study, the program could be modified for segmentation of other periodic structures, CaP bone scaffolds, and micro-CT settings.

The ability to segment all pixels in the samples made possible the novel analysis of the data in Chapter 2. For example, bone distribution was determined as a continuous function of position in the sample. Previously, histologic measures would be used, which would make impossible such measurements. The specific surface area of bone was calculated, allowing for correlations to be made between treatments and bone morphology. These measurements made possible by the program, in turn, led to a quantitative definition of "healing" that can potentially be used in comparing and evaluating scaffolds from a wide range of studies.

Chapter 4. Summary, Conclusions, and Future Work

This porcine *in vivo* study has the potential to impact scaffold design and evaluation of scaffold success for scaffold-based bone replacement and repair. The study identified specific effects of microporosity and BMP-2 on bone formation in hydroxyapatite scaffolds. The rich data set from this study demanded the creation of a fast and accurate method of material segmentation for micro-CT images, and led to the development of a new quantitative evaluation process for bone formation and scaffold success.

4.1 Demonstration of the effects of microporosity on bone formation

One of the initial objectives of the *in vivo* study was to evaluate the effect of microporosity on bone formation in an osseous site. Previous work with nearly identical scaffolds implanted intramuscularly indicated a significant benefit to bone formation with the inclusion of microporosity (40). Work with other CaP scaffolds also suggested that microporosity was beneficial to bone formation in osseous defects (14,15,31). This work demonstrated:

1. Microporosity increased bone formation and decreased the time needed to reach a steady-state volume of bone.
2. Microporosity improved bone distribution throughout the scaffold, i.e. microporosity promoted more uniform bone distribution and decreased the time needed for the distribution to reach steady-state.
3. Microporosity decreased healing time by a factor of two when compared to samples without microporosity, with “healing” defined in 2.2.6.5. Samples with microporosity healed in the same time as samples with BMP-2.

4. Microporosity promoted bone formation without affecting the cellular or metabolic activity levels of the cells; data showed the microporosity had no influence on bone specific surface area, which is a measure of metabolic activity of cells.

4.2 Demonstration of the effects of BMP-2 on bone formation

The second initial objective of the porcine study was to assess the effect of BMP-2 on bone formation in osseous sites. BMP-2 was a known osteoinductive agent (50,52-57) and, when included in scaffolds with microporosity, had previously shown effects in intramuscular sites (40). However, BMP-2's effects on osseous defects were not known, nor were the effects of BMP-2 on separate aspects of bone formation in scaffolding. This work demonstrated:

1. BMP-2 improved bone distribution throughout the scaffold and decreased the time needed for the distribution to reach steady-state. However, the effect of BMP-2 on bone distribution was not as significant as the effect of microporosity.
2. BMP-2 increased the cellular or metabolic activity levels of the cells as indicated by the increased specific surface areas of the bone formed.
3. BMP-2 decreased healing time by a factor of four when compared to samples without BMP-2, and the healing time for scaffolds containing BMP-2 was equal to those with microporosity.
4. BMP-2 did not affect the total volume fraction of bone formed for this animal defect model.

4.3 Development of segmentation algorithm for quantitative bone evaluation

A critical objective for this thesis was to develop a micro-CT segmentation algorithm to fully utilize and characterize the data obtained from the *in vivo* study. Accurate segmentation

algorithms for three material labeling – fluid/soft tissue, bone, and hydroxyapatite – previously did not exist for micro-CT images. The resulting algorithm had the following attributes and advantages:

1. The average segmentation accuracy was 94.2% ± 3.3%, volume fraction of materials determined with the algorithm were statistically identical to manual segmentation, and the pixel-by-pixel accuracy was 88.2% ± 9.5%.
2. The algorithm was very efficient; it required approximately 1 hour to segment 900 images.
3. The algorithm labeled every pixel allowing for multiple measures of bone formation including bone volume fraction, bone distribution, and bone specific surface area.

4.4 Future work

The results of the effect of microstructure and BMP-2 suggest that each scaffold design factor effects different aspects of bone formation and that those factors can be used to tailor scaffold properties for specific sites; controlling bone volume, distribution, and shape to increase healing rates. However, these factors have yet to be optimized and the mechanisms behind their effectiveness are not fully understood. Understanding why microporosity affects bone formation will greatly decrease the time needed to optimize the factor. Current theories for the effect of microstructure include micropore size, micropore fraction, and surface roughness (14,15,42,95). Understanding the possible synergistic relationship between microstructure and BMP-2 would aid in economic scaffold design as the expensive growth factor would only be used as needed. Finally, the effects of each factor could be better identified if larger scaffolds were tested as the demands of healing critical size defects would most likely emphasize the specific effects of each factor.

The micro-CT segmentation algorithms could be improved and generalized for application to other periodic structures. While the automatic segmentation developed in this work greatly reduces the amount of manual input, the initial pre-processing rotation to align the scaffold could potentially be removed. The addition of a Hough transform to the algorithm (100) may facilitate identification of scaffold orientation without any manual rotation. Adjustments could potentially be made to expand the segmentation to accommodate honeycomb-like structures as well as orthogonal ones. More accurate segmentation of the DTS images could possibly be achieved through machine learning. Finally, local differences between pixel intensities of scaffold and bone could be utilized by a watershed algorithm (66), though correction of the expected over-segmentation would need to be addressed.

Appendix – Matlab Codes

A.1 batch_seg

```
mkdir labeled
mkdir matlab

files = dir('*.tif')

for i=1:size(files,1)
    disp(strcat('Running on ', files(i).name))
    autoseg3(files(i).name);
end
```

A.2 autoseg3

```
function [im,

imlabel,imtest,ztback,ztscaff_ver,ztscaff_hor,rows,cols,scaffhor,scaffv

er] = autoseg3(filename)


    tic

    %% Reading image. %%%%%%%%%%%%%%%%%%%%%%%%%%%%%%%%%%%%%%%%%%%%%%%
    imcolor = imread(filename);
    %im = rgb2gray(imcolor);
    im = gray2ind(imcolor, 256);

    %% Crop Image %%%%%%%%%%%%%%%%%%%%%%%%%%%%%%%%%%%%%%%%%%%%%%%%%%%
    a = get_cylinder(im, 5000*256/60000);

    %%%%%%%%%%%%%%%%%%%%%%%%%%%%%%%%%%%%%%%%%%%%%%%%%%%%%%%%%%%%%%%%%%
    disp('Selecting optimal theshold for background feature.')
    % Serialize image.
    imser = double(im(:));

    % Create histogram.
    [Hist, hx] = hist(imser, min(imser):max(imser));

    % Auto threshold.
    ztback = autothresh(Hist, hx);

    disp(['Threshold: ', num2str(ztback)])

    %%%%%%%%%%%%%%%%%%%%%%%%%%%%%%%%%%%%%%%%%%%%%%%%%%%%%%%%%%%%%%%%%%
    disp('Selecting orientation(s) of the scaffold.')

    % vertical scaffold
    imtest = imfilter(im, ones(300,1)/(300));
    cols = (sum(imtest)./(size(im,1)));

    [Hist,hx] = hist(cols(cols~=0),unique(cols(cols~=0)));
    t = autothresh(Hist, hx);
    diff = [0, cols>t] - [cols>t, 0];
    scaffver = sum(diff==1)>2;

    % horizontal scaffold
    imtest = imfilter(im, ones(1,300)/(300));
    cols = (sum(imtest')./(size(im,2)));

    [Hist,hx] = hist(cols(cols~=0),unique(cols(cols~=0)));
    t = autothresh(Hist, hx);
    diff = [0, cols>t] - [cols>t, 0];
    scaffhor = sum(diff==1)>2;
```

```
      disp('Selecting optimal threshold for row feature.')

      % Compute row sums of filtered image.

       im2 = imfilter(im,ones(10,10)./(10*10));
       im2(~a) = 0;
       rows = ceil(sum(im2')./sum(a'));
       rows(isnan(rows)) = 0;

       cols = ceil(sum(im2)./sum(a));
       cols(isnan(cols)) = 0;

      % Create histogram.
      if scaffhor
          [Hist, hx] = hist(rows(rows~=0), unique(rows));
          ztscaff_hor = autothresh(Hist,hx);
      else
          ztscaff_hor = 0;
      end

      if scaffver
          [Hist, hx] = hist(cols(cols~=0), unique(cols));
          ztscaff_ver = autothresh(Hist,hx);
      else
          ztscaff_ver = 0;
      end

       disp(['Thresholds: ', num2str(ztscaff_hor), ' ',
num2str(ztscaff_ver)])

    %%%%%%%%%%%%%%%%%%%%%%%%%%%%%%%%%%%%%%%%%%%%%%%%%%%%%%%%%%%%%%%%%%%%
    disp('Labelling image.')

    [imlabel, num_pixels] = label_image(im, rows, cols, ztback,
ztscaff_hor, ztscaff_ver, a);
%     figure; imshow(im);
%     figure; imshow(immark);

    fsplit = regexp(filename, '\.', 'split');
    imwrite(imlabel, char(strcat('labeled/', fsplit(1), '_labeled.',
fsplit(2))), 'tif');
    imwrite(imcolor, char(strcat('matlab/', fsplit(1), '_matlabified.',
fsplit(2))), 'tif');

    disp('Pixels: ')
    disp(num_pixels)
    disp('Percentages: ')
    disp(num_pixels./sum(num_pixels))
    disp('Bone Scaffold, Background, Bone Growth')
end
```

A.3 get_cylinder

```
function [a] = get_cylinder(f, thres)

    h = zeros(size(f,1), size(f,2));
    h(1,:) = 1;
    h(:,1) = 1;
    h(size(f,1),:) = 1;
    h(:,size(f,2)) = 1;

    for i=2:size(f,1)
        for j = 2:size(f,2)
            if (f(i,j) < thres && h(i-1,j) && h(i,j-1))
                h(i,j) = 1;
            end
        end
    end

    for i=size(f,1)-1:-1:1
        for j = size(f,2)-1:-1:1
            if (f(i,j) < thres && h(i+1,j) && h(i,j+1))
                h(i,j) = 1;
            end
        end
    end

    for i=size(f,1)-1:-1:1
        for j = 2:size(f,2)
            if (f(i,j) < thres && h(i+1,j) && h(i,j-1))
                h(i,j) = 1;
            end
        end
    end


    for i=2:size(f,1)
        for j = size(f,2)-1:-1:1
            if (f(i,j) < thres && h(i-1,j) && h(i,j+1))
                h(i,j) = 1;
            end
        end
    end

    a = ~h;

end
```

A.4 autothresh

```
% Take as input a histogram and corresponding vector that
% specifies the value of each of the bins.
function [ztopt] = autothresh(Hist, Bins)

    % Initialize variables storing optimal threshold and
    % within-group variance at that threshold, up to this point.
    ztopt = 0;
    owopt = 1000000000;
    u0opt = 0;
    u1opt = 0;

    % Iterate over all possible threshold values and select
    % the optimal threshold w.r.t. within group variance.
    P = Hist./sum(Hist);
    for zt = Bins
       q0 = sum(P(1:find(Bins == zt)-1));
       q1 = sum(P(find(Bins == zt):size(Bins,2)));

       u0 = 0;
       o0 = 0;
       u1 = 0;
       o1 = 0;
       for z = Bins(Bins < zt)
           u0 = u0 + z * P(find(Bins == z)) / q0;
       end
       for z = Bins(Bins >= zt)
           u1 = u1 + z * P(find(Bins == z)) / q1;
       end

       for z = Bins(Bins < zt)
           o0 = o0 + (z - u0).^2 * P(find(Bins == z)) / q0;
       end
       for z = Bins(Bins >= zt)
           o1 = o1 + (z - u1).^2 * P(find(Bins == z)) / q1;
       end

       ow = q0*o0+q1*o1;
       if ow < owopt
           owopt = ow;
           ztopt = zt;
           u0opt = u0;
           u1opt = u1;
       end
    end

end
```

A.5 label_image

```
function [imlabel, num_pixels] = label_image(im, rows, cols, ztback,

ztscaff_hor, ztscaff_ver, a)

    % labels for export to amira
    % 0 - cropped
    % 1 - background
    % 2 - scaffold
    % 3 - bone
    imlabel = zeros(size(im,1),size(im,2));

    % Store the pixel counts for each group.
    % 1. background
    % 2. bone scaffold
    % 3. bone growth
    num_pixels = zeros(1,3);

    for i = 1:size(im,1)
        for j = 1:size(im,2)
            if ~a(i,j)
                imlabel(i,j) = 0;
            else if im(i,j) > ztback
                    if (rows(i) > ztscaff_hor && ztscaff_hor ~= 0) ||
(cols(j) > ztscaff_ver && ztscaff_ver ~= 0)
                        % bone scaff
                        num_pixels(1)=num_pixels(1)+1;
                        imlabel(i,j) = 2;
                    else
                        % bone growth
                        num_pixels(3)=num_pixels(3)+1;
                        imlabel(i,j) = 3;
                    end
                else
                    if im(i,j) > 2/3*ztback && ((i>0 && imlabel(i-1,j)
== 3)||(j>0 && imlabel(i,j-1) == 3))
                        % bone growth
                        num_pixels(3)=num_pixels(3)+1;
                        imlabel(i,j) = 3;
                    else
                        % background
                        num_pixels(2)=num_pixels(2)+1;
                        imlabel(i,j) = 1;
                    end
                end
            end
        end

        for i = 1:size(im,1)
            for j = 1:size(im,2)
                if a(i,j) && imlabel(i,j) == 1 && im(i,j) > 2/3*ztback
&& ((i<size(im,1) && imlabel(i+1,j) == 3)||(j<size(im,2) &&
imlabel(i,j+1) == 3))
                    num_pixels(2) = num_pixels(2)-1;
```

```
                num_pixels(3)=num_pixels(3)+1;

                imlabel(i,j) = 3;
            end
        end
    end

    imlabel = cast(imlabel,'uint8');
end
```

A.6 simplefeatures

```
mkdir eightfeatures


filesim = dir('*.tif');
filesmlab = dir('labeled/');


for i=1:size(filesim,1)
    tic
    disp(strcat('Running on ', filesim(i).name))
    [ztback, ztscaff_ver, ztscaff_hor, scaffhor, scaffver] =
paramget(filesim(i).name);
    mlab=filesmlab(i+2).name;


    filename=filesim(i).name;
    filename2=strcat('labeled/', filesmlab(i+2).name);

    image=imread(filename);
    label=imread(filename2);
    features=struct('image',image,'labels',label,'threshbg',ztback,...
        'threshver',ztscaff_ver,'threshhor',ztscaff_hor,'scaffhor',...
        scaffhor,'scaffver',scaffver);

    fsplit = regexp(filename, '\.', 'split');
    filename_final=char(strcat('eightfeatures/', fsplit(1), fsplit(2),
'_features.'));
    save(filename_final, 'features');
    toc
end
```

A.7 paramget

```
function [ztback,ztscaff_ver,ztscaff_hor,scaffhor,scaffver] =

paramget(filename)



    %% Reading image. %%%%%%%%%%%%%%%%%%%%%%%%%%%%%%%%%%%%%%%%%%%%%%%%
    imcolor = imread(filename);
    %im = rgb2gray(imcolor);
    im = gray2ind(imcolor, 256);

    %% Crop Image %%%%%%%%%%%%%%%%%%%%%%%%%%%%%%%%%%%%%%%%%%%%%%%%%%%%
    a = get_cylinder(im, 5000*256/60000);

    %%%%%%%%%%%%%%%%%%%%%%%%%%%%%%%%%%%%%%%%%%%%%%%%%%%%%%%%%%%%%%%%%%%
    disp('Selecting optimal theshold for background feature.')
    % Serialize image.
    imser = double(im(:));

    % Create histogram.
    [Hist, hx] = hist(imser, min(imser):max(imser));

    % Auto threshold.
    ztback = autothresh(Hist, hx);

    disp(['Threshold: ', num2str(ztback)])

    %%%%%%%%%%%%%%%%%%%%%%%%%%%%%%%%%%%%%%%%%%%%%%%%%%%%%%%%%%%%%%%%%%%
    disp('Selecting orientation(s) of the scaffold.')

    % vertical scaffold
    imtest = imfilter(im, ones(300,1)/(300));
    cols = (sum(imtest)./(size(im,1)));

    [Hist,hx] = hist(cols(cols~=0),unique(cols(cols~=0)));
    t = autothresh(Hist, hx);
    diff = [0, cols>t] - [cols>t, 0];
    scaffver = sum(diff==1)>2;

    % horizontal scaffold
    imtest = imfilter(im, ones(1,300)/(300));
    cols = (sum(imtest')./(size(im,2)));

    [Hist,hx] = hist(cols(cols~=0),unique(cols(cols~=0)));
    t = autothresh(Hist, hx);
    diff = [0, cols>t] - [cols>t, 0];
    scaffhor = sum(diff==1)>2;

     disp('Selecting optimal threshold for row feature.')
```

```
        % Compute row sums of filtered image.

         im2 = imfilter(im,ones(10,10)./(10*10));
         im2(~a) = 0;
         rows = ceil(sum(im2')./sum(a'));
         rows(isnan(rows)) = 0;

         cols = ceil(sum(im2)./sum(a));
         cols(isnan(cols)) = 0;

        % Create histogram.
        if scaffhor
            [Hist, hx] = hist(rows(rows~=0), unique(rows));
            ztscaff_hor = autothresh(Hist,hx);
        else
            ztscaff_hor = 0;
        end

        if scaffver
            [Hist, hx] = hist(cols(cols~=0), unique(cols));
            ztscaff_ver = autothresh(Hist,hx);
        else
            ztscaff_ver = 0;
        end

end
```

A.8 toughfix

```
function [] = toughfix(longpath)


mkdir trickyfix


files=dir('eightfeatures/');
num=size(files,1);

for i=6:num-3

    tic

    filename=files(i).name;
    filename2=files(i+1).name;
    filename3=files(i-1).name;
    filename4=files(i+2).name;
    filename5=files(i-2).name;

    name=strcat(longpath, filename);
    name2=strcat(longpath, filename2);
    name3=strcat(longpath, filename3);
    name4=strcat(longpath, filename4);
    name5=strcat(longpath, filename5);

    disp(strcat('Running on ', files(i).name))

    load(name, '-mat');
    cfeatures=features;
    cimage=cfeatures.image;
    clabels=cfeatures.labels;
    cscaffhor=cfeatures.scaffhor;
    cscaffver=cfeatures.scaffver;


    load(name2, '-mat');
    nfeatures=features;
    nlabels=nfeatures.labels;
    nscaffhor=nfeatures.scaffhor;
    nscaffver=nfeatures.scaffver;

    load(name3, '-mat');
    pfeatures=features;
    plabels=pfeatures.labels;
    pscaffhor=pfeatures.scaffhor;
    pscaffver=pfeatures.scaffver;

    load(name4, '-mat');
    nnfeatures=features;
    nnlabels=nnfeatures.labels;
```

```
load(name5, '-mat');
ppfeatures=features;
pplabels=ppfeatures.labels;


cimsize=size(cimage);

newlabel=clabels;

rowdcount=0;
coldcount=0;

bone=length(find(clabels==3));
scaff=length(find(clabels==2));
bg=length(find(clabels==2));

nbone=length(find(nlabels==3));
nscaff=length(find(nlabels==2));
nbg=length(find(nlabels==1));

pbone=length(find(plabels==3));
pscaff=length(find(plabels==2));
pbg=length(find(plabels==1));

total=bone+scaff+bg;
bf=bone/total;

ntotal=nbone+nscaff+nbg;
nsf=nscaff/ntotal;

ptotal=pbone+pscaff+pbg;
psf=pscaff/ptotal;


set=bf*4;
sets=bf*4;

dnum=0.15;

 for j=1:cimsize(1)
    cnumbone=length(find(clabels(j,:)==3));
    cnumscaff=length(find(clabels(j,:)==2));
    cnumbg=length(find(clabels(j,:)==1));

    nnumbone=length(find(nlabels(j,:)==3));
    nnumscaff=length(find(nlabels(j,:)==2));
    nnumbg=length(find(nlabels(j,:)==1));

    pnumbone=length(find(plabels(j,:)==3));
    pnumscaff=length(find(plabels(j,:)==2));
    pnumbg=length(find(plabels(j,:)==1));
```

```
        nnnumbone=length(find(nnlabels(j,:)==3));
        nnnumscaff=length(find(nnlabels(j,:)==2));
        nnnumbg=length(find(nnlabels(j,:)==1));

        ppnumbone=length(find(pplabels(j,:)==3));
        ppnumscaff=length(find(pplabels(j,:)==2));
        ppnumbg=length(find(pplabels(j,:)==1));


        if ((cnumbone/(cnumscaff+cnumbg+cnumbone))>(set) &&
((nnumscaff/(nnumbone+nnumbg+nnumscaff))>(sets))&&
((nnnumscaff/(nnnumbone+nnnumbg+nnnumscaff))>(sets)) && nscaffhor==1&&
(nsf-psf)>dnum)...
                || ((cnumbone/(cnumscaff+cnumbg+cnumbone))>(set) &&
((pnumscaff/(pnumbone+pnumbg+pnumscaff))>(sets))&&
((ppnumscaff/(ppnumbone+ppnumbg+ppnumscaff))>(sets)) &&
pscaffhor==1&&(psf-nsf)>dnum)

            for k=1:cimsize(2)
                if clabels(j,k)==3
                    newlabel(j,k)=2;
                    rowdcount=rowdcount+1;
                end
            end
        end
    end

    for k=1:cimsize(2)

        cnumbone=length(find(clabels(:,k)==3));
        cnumscaff=length(find(clabels(:,k)==2));
        cnumbg=length(find(clabels(:,k)==1));

        nnumbone=length(find(nlabels(:,k)==3));
        nnumscaff=length(find(nlabels(:,k)==2));
        nnumbg=length(find(nlabels(:,k)==1));

        pnumbone=length(find(plabels(:,k)==3));
        pnumscaff=length(find(plabels(:,k)==2));
        pnumbg=length(find(plabels(:,k)==1));

        nnnumbone=length(find(nnlabels(:,k)==3));
        nnnumscaff=length(find(nnlabels(:,k)==2));
        nnnumbg=length(find(nnlabels(:,k)==1));

        ppnumbone=length(find(pplabels(:,k)==3));
        ppnumscaff=length(find(pplabels(:,k)==2));
        ppnumbg=length(find(pplabels(:,k)==1));


            if ((cnumbone/(cnumscaff+cnumbg+cnumbone))>(set) &&
((nnumscaff/(nnumbone+nnumbg+nnumscaff))>(sets))&&
((nnnumscaff/(nnnumbone+nnnumbg+nnnumscaff))>(sets)) && nscaffver==1&&
(nsf-psf)>dnum)...
```

```
                || ((cnumbone/(cnumscaff+cnumbg+cnumbone))>(set) &&
((pnumscaff/(pnumbone+pnumbg+pnumscaff))>(sets))&&
((ppnumscaff/(ppnumbone+ppnumbg+ppnumscaff))>(sets)) &&
pscaffver==1&&(psf-nsf)>dnum)

            for j=1:cimsize(1)
                if clabels(j,k)==3
                    newlabel(j,k)=2;
                    coldcount=coldcount+1;
                end
            end
        end
    end
    for j=1:cimsize(1)
        for k=1:cimsize(2)

            if clabels(j,k)==2 && nlabels(j,k)~=2 && plabels(j,k)~=2

                newlabel(j,k)=3;
            end
        end
    end


%%%%%%%%%%%%%%%%%%%%%%%%%%%%%%%%%%%%%%%%%%%%%%%%%%%%%%%%%%%%%%%%%%%%%%%%%%%%%%%

    rowdcount
    coldcount

    fsplit=regexp(filename, '\.', 'split');
    imwrite(newlabel, char(strcat('trickyfix/', fsplit(1),
'_fixed.')),'tif');

    toc
end
```

References

1. Health and Nutrition. US Census Bureau Statisical Abstracts of the United States 2006.

2. Population. US Census Bureau Statisical Abstracts of the United States 2006.

3. Laurencin CT, Khan Y. Bone Grafts and Bone Graft Substitutes: A Brief History. In: Bone Graft Substitutes. West Conshohoken, PA: ASTM International; 2003. p. 3-10.

4. Greenwald AS, Boden SD, Goldberg VM, Yaszemski M, Heim CS. Bone-Graft Substitutes: Facts, Fictions, and Applications. In: American Academy of Orthopadeic Surgeons. San Francisco, California: 2008.

5. Schwartz CE, Martha JF, Kowalski P, Wang DA, Bode R, Li L, et al. Prospective evaluation of chronic pain associated with posterior autologous iliac crest bone graft harvest and its effect on postoperative outcome. Health and Quality of Life Outcomes. 2009;7:49.

6. Silber J, Anderson D, Daffner S, Brislin B, Leland J, Hilibrand A, et al. Donor site morbidity after anterior iliac crest bone harvest for single level anterior cervical discectomy and fusion. Spine. 2003;28:134-139.

7. LeGeros RZ. Calcium phosphate-based osteoinductive materials. Chem. Rev. 2008;108:4742-4753.

8. LeGeros R, Parsons J, Daculsi G, Driessens F, Lee D, Liu S, et al. Significance of the porosity and physical chemistry of calcium phosphate ceramics biodegradiation-bioresorption. Ann New York Acad Sci. 2006;523(Bioceramics: Material Characteristics Versus in Vivo Behavior):268-271.

9. LeGeros RZ. Properties of osteoconductive biomaterials: calcium phosphates. Clin Orthop and Rel Res. 2002;395:81.

10. CDC. Update: Unexplained Deaths Following Knee Surgery. MMWR 2001; 50(48): 1080.

11. Centers for Medicare and Medicaid Services OotAaUDoC, Bureau of Economic Analysis and Bureau of Census. National Health Expenditures, Aggregate and Per Capita Amounts, and Share of Gross Domestic Product, Selected Calendar Years 1993-2014.

12. Sloviter RS. Permanently altered hippocampal structure, excitability, and inhibition after experimental status epilepticus in the rat: the “dormant basket cell” hypothesis and its possible relevance to temporal lobe epilepsy. Hippocampus. 1991;1(1):41–66.

13. Urist M. Bone: formation by autoinduction. Science. 1965;150:893-899.

14. Hing KA, Best SM, Tanner KE, Bonfield W, Revell PA. Mediation of bone ingrowth in porous hydroxyapatite bone graft substitutes. J Biomed Mater Res Part A. 2003;68A:187-200.

15. Habibovic P, Yuan H, van der Valk CM, Meijer G, van Blitterswijk CA, de Groot K. 3D microenvironment as essential element for osteoinduction by biomaterials. Biomaterials. 2005;26:3565–3575.

16. Jarcho M. Calcium phosphate ceramics as hard tissue prosthetics. Clin Orthop and Rel Res. 1981;157:259.

17. Agrawal C, Niederauer G, Micallef D, Athanasiou K. The use of PLA-PGA polymers in orthopaedics. In: Encyclopedic handbook of biomaterials and bioengineering. New York: Marcel Dekker; 1995. p. 2081-2115.

18. Sikavitsas VI, van den Dolder J, Bancroft GN, Jansen JA, Mikos AG. Influence of the in vitro culture period on the in vivo performance of cell/titanium bone tissue-engineered constructs using a rat cranial critical size defect model. J Biomed Mater Res A. 2003;67:944-951.

19. Spoerke ED, Murray NG, Li H, Brinson C, Dunand DC, Stupp SI. A bioactive titanium foam scaffold for bone repair. Acta Biomaterialia. 2005;1:523-533.

20. Ducheyne P, Radin S, King L. The effect of calcium phosphate ceramic composition and structure on in vitro behavior. I. Dissolution. J Biomed Mater Res. 1993;27:25-34.

21. Habibovic P, Sees TM, van den Doel MA, van Blitterswijk CA, de Groot K. Osteoinduction by biomaterials - physicochemical and structural influences. Journal of biomedical materials and research part a. 2006;77A:747-762.

22. Albrektsson T, Johansson C. Osteoinduction, osteoconduction and osseointegration. European Spine Journal. 2001;10:96–101.

23. Hutmacher DW. Scaffold design and fabrication technologies for engineering tissues state of the art and future perspectives. Journal of Biomaterials Science, Polymer Edition. 2001;12(1):107–124.

24. Zhao Y, Zhang J, Wang X, Chen B, Xiao Z, Shi C. The osteogenic effect of bone morphogenetic protein-2 on the collagen scaffold conjugated with antibodies. J Control Release. 4 Jun 2009.

25. Holland TA, Mikos AG. Review: Biodegradable polyermic scaffolds.

Improvements in bone tissue engineering through controlled drug deliver. Adv Biochem Eng Biotechnol. 2006;102:161-185.

26. Ramakrishna S, Mayer J, Wintermantel E, Leong KW. Biomedical applications of polymer-composite materials: a review. Composites Science and Technology. 2001;61(9):1189–1224.

27. Gronthos S, Brahim J, Li W, Fisher L, Cherman N, Boyde A, et al. Stem Cell Properties of Human Dental Pulp Stem Cells. Journal of Dental Research. 2002;81:531-535.

28. Hubbell J. Biomaterials in tissue engineering. Nature Biotechnology. 1995;13:565-575.

29. Koyama T, Handa J. Porous hydroxyapatite ceramics for use in neurosurgical practice. Surg Neurol. 1986;25:71-73.

30. Kawasaki T. Hydroxyapatite as a liquid-chromatographic packing. J Chromatogr. 544:147-184.

31. Hing K, Annaz B, Saeed S, Revell P, Buckland T. Microporosity enhances bioactivity of synthetic bone graft substitutes. J Mater Sci:Mater in Med. 2005;16:467-475.

32. Hoelzle DJ, Alleyne AG, Wagoner Johnson AJ. Micro-robotic deposition guidelines by a design of experiments approach to maximize fabrication reliability for the bone scaffold application. Acto Biomaterialia. 2008;4:897-912.

33. Wakae H, Takeuchi A, Matsuya S, Munar M, LeGeros R, Nakasima A, et al. Fabrication of macroporous carbonate apatite foam by hydrothermal conversion of alpha-tricalcium phosphate in carbonate solutions. J Biomed MaterRes Part A. 2008;87A:957-963.

34. Nery EB, Lynch KL, Pflughoeft FA, Rooney GE. Functional loading of bioceramic augmented alveolar ridge: A pilot study. Prosthet Dent. 1978;43:338-343.

35. Geesink RGT. Experimental and clinical experience with hydroxyapatite-coated hip implants. Orthopedics. 1989;12:1239-1243.

36. Cook SD, Thomas KF, Dalton JE, Volkman TK, Whitecloud TS, Kay JF. Hydroxylapatite coating of porous implants improves bone ingrowth and interface attachment strength. J Biomed Mater Res. 1992;26:989-1001.

37. An Y, Woolf S, Friedman R. Pre-clinical in vivo evaluation of orthopaedic bioabsorbable devices. Biomaterials. 2000;21:2635-2652.

38. Lan Levengood SK, Polak SJ, Wheeler MB, Maki AJ, Clark SG, Jamison RD, et al. Multiscale osteointegration as a new paradigm for the design of calcium phosphate scaffolds for bone regeneration. Biomaterials. 2010;31:3552-3563.

39. Hing KA. Bioceramic bone graft substitutes: influence of porosity and chemistry. Int J Appl Ceram Technol. 2005;2(3):184-199.

40. Woodard JR, Hilldore AJ, Lan SK, Park C, Morgan AW, Eurell JAC, et al. The mechanical properties and osteoconductivity of hydroxyapatite bone scaffolds with multi-scale porosity. Biomaterials. 2007;28:45-54.

41. Habibovic P, de Groot K. Osteoinductive biomaterials—properties and relevance in bone repair. J Tissue Eng Regen Med. 2007;1:25-32.

42. Karageorgiou V, Kaplan D. Porosity of 3D biomaterial scaffolds and osteogenesis. Biomaterials. 2005;(27):5474–5491.

43. Oonishi H, Hench LL, Wilson J, Sugihara F, Tsuji E, Kushitani S, et al. Comparative bone growth behavior in granules of bioceramic materials of various sizes. J Biomed Mater Res. 1999;44:31-43.

44. Sela J, Gross UM, Kohavi D, Shani J, Dean DD, Boyan BD, et al. Primary mineralization at the surface of implants. Crit Rev Oral Biol Med. 2000;11:423-436.

45. Kim YG, Seo DS, Lee JK. Comparison of dissolution resistance in artificial hydroxyapatite and biologically derived hydroxyapatite ceramics. J Phys and Chem of Solids. 2008;69.

46. Seo DS, Lee JK. Microstructural disintegration in dense hydroxyapatite and hydroxyapatite-coated metal implants. Metals and Materials Int. 13:311-316.

47. Seo DS, Kim H, Hwang KH, Lee JK. Dissolution and mechanical properties of sintered hydroxyapatite immersed in water. In: Science of Engineering Ceramics III, Key engineering materials. 2006. p. 789-792.

48. Kruyt MC, de Bruijn JD, Yuan H, van Blitterswijk CA, Verbout AJ, Oner FC, et al. Optimization of bone tissue engineering in goats: a peroperative seeding method using cryopreserved cells and localized bone formation in calcium phosphate scaffolds1. Transplantation. 2004;77(3):359-365.

49. Le Huec J, Clement D, Brouillaud B, Barthe N, Dupuy B, Foliguet B, et al. Evolution of the local calcium content around irradiated b-tricalcium phosphate ceramic implants: in vivo study in the rabit. Biomaterials. 1998;19:733-738.

50. Cheng H, Jiang W, Phillips FM, Haydon RC, Peng Y, Zhou L, et al. Osteogenic activity of the fourteen types of human bone morphogenetic proteins (BMPs). J

Bone Joint Surg Am. 2003;85A(8):1544-1552.

51. Lan Levengood SK, Polak SJ, Poellmann MJ, Hoelzle DJ, Maki AJ, Clark SG, et al. The effect of BMP-2 on micro- and macroscale osteointegration of biphasic calcium phosphate scaffolds with multiscale porosity. Acto Biomaterialia. 2010;6:3283-3291.

52. Wang EA, Rosen V, D'Alessandro JS, Bauduy M, Cordes P, Harada T, et al. Recombinant human bone morphogenetic protein induces bone formation. Proc Natl Acad Sci. 1990;87:2220-2224.

53. Cao X, Chen D. The BMP signaling and in vivo bone formation. Gene. 2005;357:1–8.

54. Tsumaki N, Yoshikawa H. The role of bone morphogenetic proteins in endochondral bone formation. Cytokine and Growth Factor Reviews. 2005;16:279–285.

55. Reddi AH, Cunningham NS. Initiation and promotion of bone differentiation by bone morphogenetic proteins. J Bone and Mineral Res. 1993;8(2):S499-S502.

56. Reddi AH. Bone morphogenetic proteins: an unconventional approach to isolation of first mammalian morphogens. Cytokine & Growth Factor Reviews.

1997;8(1):11–20.

57. Onishi T, Ishidou Y, Nagamine T, Yone K, Imamura T, Kato M, et al. Distinct and overlapping patterns of localization of bone morphogenetic protein (BMP) family members and a BMP type II receptor during fracture healing in rats. Bone. 1998;22(6):605–612.

58. Reddi AH. Bone and cartilage differentiation. Current Opinion in Genetics and Development. 1994;4:737-744.

59. Cunningham NS, Paralkar V, Reddi AH. Osteogenin and recombinant bone morphogenetic protein 2B are chemotactic for human monocytes and stimulate transforming growth factor beta 1 mRNA expression. Proceedings of the National Academy of Sciences of the United States of America. 1992;89(24):11740.

60. Lind M, Eriksen EF, B\ünger C. Bone morphogenetic protein-2 but not bone morphogenetic protein-4 and-6 stimulates chemotactic migration of human osteoblasts, human marrow osteoblasts, and U2-OS cells. Bone. 1996;18(1):53–57.

61. Sohier J, Daculsi G, Sourice S, de Groot K, Layrolle P. Porous beta tricalcium phosphate scaffolds used as a BMP-2 delivery system for bone tissue engineering. J. Biomed. Mater. Res. 2009;92A:1105-1114.

62. DiMarcantonio T. BMP-2 and BMP-7 continue to show success in long bone fractures and nonunions. Orthopedics Today. Oct 2006.

63. Keller C. Methods, Compositions and Systems for Analyzing Imaging Data. 2007.

64. Forsyth DA, Ponce J. Computer Vision: A Modern Approach. Prentice Hall; 2002.

65. Zhang J, Yan CH, Chui CK, Ong SH. Fast segmentation of bone in CT images using 3D adaptive thresholding. Computers in Biology and Medicine. 2010;40(2):231–236.

66. Meyer F, Beucher S. Morphological segmentation. Journal of visual communication and image representation. 1990;1(1):21–46.

67. Hollister SJ, Lin CY, Saito E, Schek RD, Taboas JM, Williams JM, et al. Engineering craniofacial scaffolds. Orthodontics & craniofacial research. 2005;8(3):162–173.

68. van Lenthe GH, Hagenm\üller H, Bohner M, Hollister SJ, Meinel L, M\üller R. Nondestructive micro-computed tomography for biological imaging and quantification of scaffold-bone interaction in vivo. Biomaterials. 2007;28(15):2479–2490.

69. Gauthier O, M\üller R, von Stechow D, Lamy B, Weiss P, Bouler JM, et al. In vivo bone regeneration with injectable calcium phosphate biomaterial: a three-dimensional micro-computed tomographic, biomechanical and SEM study. Biomaterials. 2005;26(27):5444–5453.

70. Taboas JM, Maddox RD, Krebsbach PH, Hollister SJ. Indirect solid free form fabrication of local and global porous, biomimetic and composite 3D polymer-ceramic scaffolds. Biomaterials. 2003;24(1):181–194.

71. von Doernberg MC, von Rechenberg B, Bohner M, Gr\ünenfelder S, van Lenthe GH, M\üller R, et al. In vivo behavior of calcium phosphate scaffolds with four different pore sizes. Biomaterials. 2006;27(30):5186–5198.

72. Dellinger JG, Cesarano J, Jamison RD. Robotic deposition of model hydroxyapatite scaffolds with multiple architectures and multiscale porosity for bone tissue engineering. J. Biomed. Mater. Res. 2007;82A:383-394.

73. Cordell JM. The influence of micropore size on the mechanical properties of bulk hydroxyapatite and hydroxyapatite scaffolds: University of Illinois at Urbana-Champaign; 2008.

74. Michna S, Wu W, Lewis JA. Concentrated hydroxyapatite inks for direct-write assembly of 3-D periodic scaffolds. Biomaterials. 2005;26:5632-5639.

75. Hoelzle DJ. Reliability guidelines and flowrate modulation for a micro robotic deposition system: University of Illinois at Urbana-Champaign; 2007.

76. Park CJ, Clark SG, Lichtensteiger CA, Jamison RD, Wagoner Johnson AJ. Accelerated wound closure of pressure ulcers in aged mice by chitosan scaffolds with and without bFGF. Acta Biomaterialia. 2009;5:1926-1936.

77. Morgan AW. The use of gelatin in a multiple drug delivery system: University of Illinois at Urbana-Champaign; 2006.

78. Sterchi D, Eurell J. An evaluation of methylmethacrylate mixtures for hard tissue embedding. J Histotechnol. 1995;18:45-49.

79. Abdi H. Bonferroni and Sidak corrections for multiple comparisons. In: Encyclopedia of Measurement and Statistics. Thousand Oak, CA: Sage; 2007.

80. Hill T, Lewicki P. Statistics Methods and Applications. Tulsa, OK: StatSoft; 2007.

81. Tabachnick BG, Fidell LS. Using multivariate statistics. 5th ed. Boston: Allyn and Bacon; 2007.

82. Cowin SC. Tissue growth and remodeling. Annu. Rev. Biomed. Eng. 2004;6:77-

107.

83. Warner SE, Shea JE, Miller SC, Shaw JM. Adaptations in cortical and trabecular bone in response to mechanical loading with and without weight bearing. Calcif Tissue Int. 2006;79:395-403.

84. Thomas L. Retrospective power analysis. Soc Conservation Biol. 1997;11(1):276-280.

85. Willems NM, Mulder L, Langenbach GE, Grünheid T, Zentner A, van Eijden TM. Age-related changes in microarchitecture and mineralization of cancellous bone in the porcine mandibular condyle. J Struct Biol. 2007;158:421–427.

86. Beddoe AH. A quantitative study of the structure of trabecular bone in man, rhesus monkey, beagle and miniature pig. Calc Tissue Int. 1978;25:273–281.

87. Winter G, Simpson B. Heterotopic bone formed in a synthetic sponge in the skin of young pigs. Nature. 1969;223:88-90.

88. Bostrom M, Lane J, Tomin E, Browne M, Berberian W, Turek T, et al. The use of bone morphogenetic protein-2 in the rabbit ulnar nonunion model. Clin Orthop. 1996;327:272-282.

89. Yasko A, Lane J, Fellinger E, Rosen V, Wozney J, Wang E. The healing of segmental defects, induced by recombinant human bone morphogenetic protein (rhBMP-2). A radiographic, histological, and biomechanical study in rats. J Bone Joint Surg Am. 1992;74:659-670.

90. Yamamoto M, Ikada Y, Tabata Y. Controlled release of growth factors based on biodegradation of gelatin hydrogel. J Biomater Sci, Polymer Ed. 2001;12:77-88.

91. Dai KR, Xu XL, Tang TT, .Zhu ZA, Yu CF, Lou JR, et al. Repairing of goat Tibial Bone Defects with BMP-2 Gene–Modified Tissue-Engineered Bone. Calcif Tissue Int. 77:55-61.

92. Wozney J, Rosen V. Bone morphogenetic protein and bone morphogenetic protein gene family in bone formation and repair. Clin Orthop. 1998;346:26-37.

93. Marcus R. Normal and abnormal bone remodeling in man. Ann Rev Med. 1987;38:129-141.

94. Arnett T. Update on bone cell biology. European J Orthodontics. 1990;12:81-90.

95. Yuan H, Kurashina K, de Bruijn JD, de Groot K, Zhang X. A preliminary study on osteoinduction of two kinds of calcium phosphate ceramics. Biomaterials. 1999;20:1799-1806.

96. Ducheyne P, Radin S, Heughebaert M, Heughebaert JC. Calcium phosphate ceramic coatings on porous titanium: effect of structure and composition on electrophoretic deposition, vacuum sintering and in vitro dissolution. Biomaterials. 1990;11:244–254.

97. Ding M, Odgaard A, Hvid I. Accuracy of cancellous bone volume fraction measured by micro-CT scanning. Journal of biomechanics. 1999;32(3):323–326.

98. Rajagopalan S, Lu L, Yaszemski MJ, Robb RA. Optimal segmentation of microcomputed tomographic images of porous tissue-engineering scaffolds. J. Biomed. Mater. Res. 2005 12;75A(4):877-887.

99. Staal J, van Ginneken B, Viergever MA. Automatic rib segmentation and labeling in computed tomography scans using a general framework for detection, recognition and segmentation of objects in volumetric data. Medical Image Analysis. 2007;11(1):35–46.

100. Fernandes LA, Oliveira MM. Real-time line detection through an improved Hough transform voting scheme. Pattern Recognition. 2008;41(1):299–314.